Manipulation of the unfolded protein response: a pharmacological strategy against coronavirus infection

Liliana Echavarría-Consuegra[#1], Georgia M. Cook[#1], Idoia Busnadiego[2], Charlotte Lefèvre[1], Sarah Keep[3], Katherine Brown[1], Nicole Doyle[3], Giulia Dowgier[3], Krzysztof Franaszek[1], Nathan A. Moore[4,5], Stuart G. Siddell[4], Erica Bickerton[3], Benjamin G. Hale[2], Andrew E. Firth[1], Ian Brierley[1], Nerea Irigoyen[1]*

[1]Division of Virology, Department of Pathology, University of Cambridge, Tennis Court Road, Cambridge, United Kingdom.

[2]Institute of Medical Virology, University of Zurich, Zurich, Switzerland.

[3]The Pirbright Institute, Woking, Surrey, United Kingdom.

[4]Department of Cellular and Molecular Medicine, University of Bristol, Bristol, United Kingdom.

[5]Current address: Basingstoke and North Hampshire Hospital, Hampshire Hospitals, NHS Foundation Trust.

Running Title: Targeting the unfolded protein response in coronavirus infection

[#]These authors contributed equally.

*Corresponding author: ni236@cam.ac.uk

Keywords: SARS-CoV-2, murine coronavirus, unfolded protein response, ribosome profiling, RNASeq, antiviral intervention.

Abstract

Coronavirus infection induces the unfolded protein response (UPR), a cellular signalling pathway composed of three branches, triggered by unfolded proteins in the endoplasmic reticulum (ER) due to high ER load. We have used RNA sequencing and ribosome profiling to investigate holistically the transcriptional and translational response to cellular infection by murine hepatitis virus (MHV), often used as a model for the *Betacoronavirus* genus to which the recently emerged SARS-CoV-2 also belongs. We found the UPR to be amongst the most significantly up-regulated pathways in response to MHV infection. To confirm and extend these observations, we show experimentally the induction of all three branches of the UPR in both MHV- and SARS-CoV-2-infected cells. Over-expression of the SARS-CoV-2 ORF8 or S proteins alone is itself sufficient to induce the UPR. Remarkably, pharmacological inhibition of the UPR greatly reduced the replication of both MHV and SARS-CoV-2, revealing the importance of this pathway for successful coronavirus replication. This was particularly striking when both IRE1α and ATF6 branches of the UPR were inhibited, reducing SARS-CoV-2 virion release ~1,000-fold. Together, these data highlight the UPR as a promising antiviral target to combat coronavirus infection.

Author Summary

SARS-CoV-2 is the novel coronavirus responsible for the COVID-19 pandemic which has resulted in over 100 million cases since the end of 2019. Most people infected with the virus will experience mild to moderate respiratory illness and recover without any special treatment. However, older people, and those with underlying medical problems like chronic respiratory disease are more likely to develop a serious illness. So far, more than 2 million people have died of COVID-19. Unfortunately, there is no specific medication for this viral disease.

In order to produce viral proteins and to replicate their genetic information, all coronaviruses use a cellular structure known as the endoplasmic reticulum or ER. However, the massive production and modification of viral proteins stresses the ER and this activates a compensatory cellular response that tries to reduce ER protein levels. This is termed the unfolded protein response or UPR. We believe that coronaviruses take advantage of the activation of the UPR to enhance their replication.

The UPR is also activated in some types of cancer and neurodegenerative disorders and UPR inhibitor drugs have been developed to tackle these diseases. In this work, we have tested some of these compounds in human lung cells infected with SARS-CoV-2 and found that virus production was reduced 1000-fold in human lung cells.

Introduction

The *Coronaviridae* are a family of enveloped viruses with positive-sense, non-segmented, single-stranded RNA genomes. Coronaviruses (CoVs) cause a broad range of diseases in animals and humans. SARS-CoV, MERS-CoV and SARS-CoV-2, members of the genus *Betacoronavirus*, are three CoVs of particular medical importance due to high mortality rates and pandemic capacity [1–3]. SARS-CoV-2 is the causative agent of the current COVID-19 pandemic, which has resulted in over 95 million cases and more than 2 million deaths since the end of 2019. Although 15% of the cases develop a severe pathology, no specific therapeutic treatment for COVID-19 has been approved to date, highlighting the urgent need to identify new antiviral strategies to combat SARS-CoV-2, besides future CoV zoonoses.

During CoV replication, the massive production and modification of viral proteins, as well as virion budding-related endoplasmic reticulum (ER) membrane depletion, can lead to

overloading of the folding capacity of the ER and consequently, ER stress [4]. This activates the unfolded protein response (UPR) which is controlled by three ER-resident transmembrane sensors: inositol-requiring enzyme-1 α (IRE1α), activating transcription factor-6 (ATF6), and PKR-like ER kinase (PERK), each triggering a different branch of the UPR (Fig 1A). Activation of these pathways leads to decreased protein synthesis and increased ER folding capacity, returning the cell to homeostasis [5].

Here, we characterise global changes in the host translatome and transcriptome during murine coronavirus (MHV) infection using RNA sequencing (RNASeq) and ribosome profiling (RiboSeq). MHV is a member of the *Betacoronavirus* genus and is widely used as a model to study the replication and biology of members of the genus. In this analysis, the UPR is one of the most significantly enriched pathways. We further confirm the activation of all three branches of the UPR in MHV-infected cells. Extending our investigation to SARS-CoV-2, we find that infection with this novel CoV also activates all three UPR pathways. Moreover, we demonstrate that individual over-expression of SARS-CoV-2 ORF8 and S proteins is sufficient to induce the UPR. Remarkably, pharmacological inhibition of the UPR had a dramatic negative effect on MHV and SARS-CoV-2 replication, suggesting that CoVs may subvert the UPR to their own advantage. These results reveal that pharmacological manipulation of the UPR can be used as a therapeutic strategy against coronavirus infection.

Results

Differential gene expression analysis of murine cells infected with MHV-A59

To survey genome-wide changes in host transcription and translation during CoV infection, murine 17 clone 1 cells (17 Cl-1) were infected with recombinant MHV-A59 at a multiplicity of infection (MOI) of 10, or mock-infected, in duplicate and harvested at 5 hours post-infection

100 (h p.i.). Lysates were subjected to RNASeq and parallel RiboSeq [6,7], which allows global
101 monitoring of cellular translation by mapping the positions and abundance of translating
102 ribosomes on the transcriptome with sub-codon precision. Quality control analysis confirmed
103 the libraries were of high quality (S1 Figure, S1 Table).
104
105 To assess the effects of MHV infection on cellular transcript abundance, differential expression
106 analysis was performed at 5 h p.i. with DESeq2 [8] (Fig 1B and C, S2 and S3 Tables). At this
107 timepoint, viral RNA synthesis approaches a maximum, but it precedes the onset of cytopathic
108 effects such as syncytium formation [7]. Between infected and mock-infected conditions, genes
109 with a fold change ≥2 and a false discovery rate (FDR)-corrected p value of ≤0.05 were
110 considered to be significantly differentially transcribed (S2 Table). To determine the biological
111 pathways involved in the response to infection, we carried out Reactome pathway enrichment
112 analysis [9] on the lists of significantly differentially transcribed genes (Fig 1B, S3 Table). The
113 most significantly enriched pathway associated with transcriptionally up-regulated genes was
114 "Unfolded Protein Response" (R-HSA-381119, $p = 1.1\times10^{-10}$), and pathways denoting the
115 three branches of the UPR (ATF6 branch: R-HSA-381183, PERK branch: R-HSA-380994,
116 IRE1α branch: R-HSA-381070) were also significantly enriched (S3 Table). Consistent with
117 this, gene ontology (GO) term enrichment analysis of the transcriptionally up-regulated gene
118 list revealed that UPR-related GO terms, such as "response to unfolded protein"
119 (GO:0006986), were significantly enriched (S3 Table). Many of the enriched pathways and
120 GO terms associated with transcriptionally down-regulated genes are related to protein
121 synthesis, again highlighting this as a key theme of the host response.
122
123 We provide the full database of differentially expressed genes and enriched pathways/GO
124 terms for further exploration (S2 and S3 Tables) but in this manuscript we will focus

125 predominantly on the UPR, which has been recognised as a host response to several CoVs due
126 to the extensive dependence of CoV replication on the ER [4]. Accordingly, some of the most
127 differentially transcribed genes are involved in the UPR, such as *Herp* (also known as *Herpud*),
128 *Chac1*, *Bip* (also known as *Grp78* or *Hspa5*), *Chop* (also known as *Ddit3* or *Gadd153*) and
129 *Grp94* (also known as *Hsp90b1*) (Fig 1C).
130
131 To evaluate differences at the level of translation, we calculated relative translation efficiencies
132 (TE; defined herein as the ratio of ribosome-protected-fragment [RPF] to total RNA density in
133 the CDS of a given gene) at 5 h p.i. using Xtail [10], applying the same fold change and *p*-
134 value thresholds as for the transcription analysis. As shown in Fig 1D, several of the
135 translationally up-regulated genes encode key proteins involved in activation of the UPR, for
136 example ATF4, ATF5 and CHOP, which are effector transcription factors [11–16]. GADD34
137 (also known as MYD116/PPP1R15A), a protein that acts as a negative regulator to diminish
138 prolonged UPR activation [17,18], was also translationally up-regulated.
139
140 Given that UPR activation can lead to eIF2α phosphorylation and host translational shut-off,
141 we investigated whether the list of mRNAs found to be preferentially translated during MHV
142 infection was enriched for genes resistant to translational repression by phosphorylated eIF2α
143 (p-eIF2α) (Materials and Methods, S4 Table). We found a 9.15-fold enrichment of p-eIF2α
144 resistant genes ($p = 1.42\times10^{-4}$, Fisher Exact Test). Resistance to the effects of p-eIF2α has been
145 linked to the presence of efficiently translated upstream open reading frames (uORFs) in the 5′
146 UTR [11–16,19]. To investigate this in our dataset, we analysed ribosome occupancy of the
147 main ORF compared to the uORFs on *Atf4*, a well-studied example(12) (Fig 1E). Translation
148 of the short (three codon) uORF1 was observed under all conditions. In mock-infected samples,
149 uORF2 was efficiently translated, largely precluding translation of the main ORF (pink). In

150 contrast, in MHV-infected cells, a large proportion of ribosomes scan past uORF2 to translate
151 the main ORF. This is consistent with previous studies on *Atf4* translation under conditions of
152 eIF2α phosphorylation, in which many ribosomes cannot reassemble a competent initiation
153 complex before reaching uORF2 [11,12]. This facilitates increased production of Atf4 even
154 when translation of most mRNAs is inhibited.
155
156 Comparison of the fold changes at the transcriptional and translational level for individual
157 cellular mRNAs provides insight into the overall effect on gene expression (Fig 1F). Genes
158 regulated in opposing directions transcriptionally and translationally likely result in a small
159 overall change in expression, whereas genes regulated only in one direction likely result in a
160 greater overall change. Many UPR genes fall into the latter category (orange points, top-centre
161 and right-centre), reflecting published knowledge about the induction of these genes
162 specifically at the transcriptional [20–23] or translational level [12–16,19]. *Chop* (green point,
163 upper-right) is a rare example of a gene that is significantly up-regulated both transcriptionally
164 and translationally during MHV infection. This reflects the fact that it is transcriptionally
165 induced by ATF4 during UPR activation and translationally p-eIF2α-resistant [24,25].
166
167 Together, the ribosome profiling results highlight the UPR as a key pathway in the host
168 response to MHV infection, with many of the greatest expression changes observed for UPR-
169 related genes.
170
171 **MHV infection and activation of the unfolded protein response**
172 To further explore the extent of UPR activation during MHV infection, we investigated each
173 of the three branches individually (Fig 1A), building on the work of several groups [26–30].
174

175 *Monitoring the PERK-eIF2α-ATF4 branch*

176 Upon ER stress, PERK oligomerises and auto-phosphorylates [31]. Activated PERK
177 phosphorylates the α-subunit of eIF2 which in turn impairs recycling of inactive eIF2-GDP to
178 active eIF2-GTP, resulting in a general shutdown of protein synthesis [32]. However,
179 translation of ATF4 is increased in this situation [12,33,34] leading to the induction of its target
180 genes *Chop* and *Gadd34* (Fig 1A, right). To assay PERK activation, we monitored expression
181 of PERK, CHOP, ATF4 and p-eIF2α, by qRT-PCR and western blotting. 17 Cl-1 cells were
182 infected with MHV-A59 or incubated with tunicamycin and harvested at 2.5, 5, 8 and 10 h.
183 Tunicamycin, used as a positive control, is a pharmacological inducer of ER stress which
184 activates all UPR signalling pathways. From 5 h p.i. onwards in MHV-infected cells, and at all
185 timepoints in tunicamycin-treated cells, ATF4 and p-eIF2α were detected and multiple bands
186 were observed for PERK (Fig 2A) corresponding to the auto-phosphorylated species, indicative
187 of activation of this kinase upon ER stress. In addition, as shown in Fig 2B, *Chop* and *Gadd34*
188 mRNA levels in MHV-infected cells (blue squares) increased from 2.5 to 8 h p.i., similarly to
189 tunicamycin-treated cells (red circles), indicating their induction by the transcription factor
190 ATF4.

191

192 Virus-induced inhibition of translation as a consequence of eIF2α phosphorylation was
193 confirmed by analytical polysome profiling in 17 Cl-1 cells (Fig 2C, upper panel), revealing
194 the accumulation of monosomes (80S) in MHV-infected cells at 5 h p.i. In higher salt profiles
195 (400 mM KCl; Fig 2C, lower panel), where 80S ribosomes lacking mRNA dissociate into
196 constituent subunits, a large reduction in 80S ribosomes was seen. These data are highly
197 consistent with inhibition of translation initiation and show that the vast majority of 80S
198 ribosomes accumulating at this time point are not mRNA-associated. These data support the

199 view that MHV infection leads to translational shut-off via inhibited initiation, consistent with
200 the effects of eIF2α phosphorylation.
201
202 *Monitoring the IRE1α-XBP1 branch*
203 Activated IRE1α (Fig 1A, left) removes a 26-nt intron from unspliced *Xbp1* (*Xbp1-u*) mRNA
204 leading to a translational reading frame shift and a longer protein [23,35]. The product of
205 spliced *Xbp1* mRNA (XBP1-s) is an active transcription factor that up-regulates the expression
206 of ER-associated degradation (ERAD) components and ER chaperones. To study this, we
207 analysed *Xbp1-u* and *Xbp1-s* mRNAs by reverse transcriptase PCR (RT-PCR), using specific
208 primers flanking the splice site (Fig 2D). At all timepoints, *Xbp1-u* was the predominant form
209 in mock-infected cells whereas *Xbp1-s* was the major species in tunicamycin-treated cells. In
210 virus-infected cells, *Xbp1-s* became predominant at 5 h p.i. This was corroborated at the
211 translational level in the ribosome profiling datasets, in which infected samples showed
212 increased translation of the extended ORF (yellow) generated by splicing (S2 Figure). An
213 increase in active XBP1-s transcription factor was further supported by the finding that two of
214 its target genes are transcriptionally up-regulated in infected cells (*ERdj4* – 2.44-fold increase
215 $p=6.63\times10^{-08}$; and *P58ipk* – 1.94-fold increase $p=3.97\times10^{-11}$) (S2 Table). These data indicate
216 that the IRE1α-Xbp1 pathway is activated by MHV infection.
217
218 *Monitoring the ATF6 branch*
219 The ATF6 branch is activated when ATF6 translocates from the ER to the Golgi apparatus,
220 where it is cleaved [36]. After cleavage, the amino-terminus of ATF6 (ATF6-Nt) translocates
221 to the nucleus to up-regulate ER chaperones (Fig 1A, middle). To monitor this pathway, 17 Cl-
222 1 cells were infected with MHV-A59 or incubated with tunicamycin and analysed by western
223 blotting (to detect ATF6 cleavage) or by immunofluorescence (to detect ATF6 nuclear

224 translocation) (S3A, S3B and S3C Figures). However, we were unable to detect the trimmed
225 version of ATF6 nor a clear nuclear translocation. As ATF6-Nt was also not visible in the
226 positive control tunicamycin-treated cells, it is likely that the antibodies used do not efficiently
227 recognise mouse ATF6-Nt in this context.
228
229 As an alternative approach, we monitored the induction of *BiP*, *Grp94* and *calreticulin*,
230 transcriptionally up-regulated genes in the Reactome category "ATF6 (ATF6-alpha) activates
231 chaperone genes" (S3 Table) and known to be induced by ATF6-Nt [37,38]. BiP mRNA or
232 protein levels are often used as a proxy for activation of the ATF6 pathway; however, its
233 transcription can eventually be regulated by other UPR factors such as XBP1 [39] and ATF4
234 [40], so it can also be used as general readout of ER stress [26,37]. Cells were harvested at 2.5,
235 5 and 8 h p.i. and analysed by qRT-PCR (Fig 2E). An increase in *Bip* transcription was observed
236 in tunicamycin-treated (red circles) and to a lesser extent in MHV-infected cells (blue squares)
237 from 2.5 to 8 h p.i., whereas mock-infected cells (green triangles) showed no induction. Despite
238 the transcriptional up-regulation and a noticeable increase in RiboSeq reads mapping to BiP
239 (S3D Figure), the protein was not detectable by western blot in MHV-infected cells (Fig 2F).
240 It is not yet clear why this is the case, although down-regulation of BiP at the protein level has
241 previously been observed during infection with other members of the order *Nidovirales*
242 [30,41]. Nevertheless, an increase in *calreticulin* and *Grp94* transcription (Fig 2E) was
243 observed in tunicamycin-treated cells (red circles) and to a greater extent in MHV-infected
244 cells (blue squares) especially at 8 h p.i. This indicates that the ATF6 pathway is highly up-
245 regulated during MHV-infection. Together with our studies of PERK-eIF2α-ATF4 and IRE1α-
246 Xbp1 above, these data confirm that MHV infection induces all three branches of the UPR.
247
248 **Effect of UPR inhibitors on MHV replication**

249 Based on the strong UPR activation brought about by MHV infection, we hypothesised that
250 pharmacological manipulation of this pathway could be used to modulate viral replication.
251 First, we determined cell viability after drug treatment using Cell Titre Glo and trypan blue
252 exclusion assays (S4 Figure). Subsequently, we evaluated the inhibitory effect of four different
253 UPR inhibitors (UPRi) on each one of the UPR branches in cells infected with MHV for 8 h at
254 MOI 5 (S5 Figure).
255
256 GSK-2606414 (henceforth referred to as PERKi) is a specific inhibitor of PERK [42,43]. As
257 expected, PERKi treatment prevented autophosphorylation of PERK and reduced
258 phosphorylation of its substrate, eIF2α (S5A Figure), effectively blocking this branch of the
259 UPR. Pulse labelling of infected cells for one hour at 5 h p.i. revealed a modest increase of both
260 viral and host protein synthesis, with no effect on mock-infected cells (S5B Figure). Analytical
261 polysome profiling of MHV-infected cells treated with 5 μM PERKi for 5 h (S5C Figure)
262 revealed a decrease in the accumulation of monosomes (80S) compared to MHV-infected cells
263 at 5 h p.i. (Fig 2C, upper right panel), indicating a relief of translation inhibition.
264
265 Integrated stress response inhibitor (ISRIB) acts downstream of eIF2α in the PERK pathway
266 by preventing p-eIF2α from binding and inhibiting eIF2B [44]. Therefore, eIF2B can recycle
267 eIF2-GDP to active eIF2-GTP, and translation initiation can still occur, despite the levels of p-
268 eIF2α remaining unchanged. Inhibition of the PERK pathway downstream of eIF2α is evident
269 from the decrease in *Chop* transcription in MHV-infected cells treated with 2 μM ISRIB (S5D
270 Figure).
271
272 STF-083010 (henceforth referred to as IREi) is a specific IRE1α endonuclease inhibitor that
273 does not affect its kinase activity [45]. In MHV-infected cells treated with IREi at 60 μM (8 h

274 p.i., S5E Figure) the unspliced form of Xbp1 was more prominent compared to the untreated
275 MHV-infected cells, indicating a block in the endonuclease activity of this enzyme.
276
277 AEBSF, a serine protease inhibitor, prevents ER stress-induced cleavage of ATF6 resulting in
278 inhibition of transcriptional induction of ATF6 target genes [46]. We investigated the induction
279 of ATF6 target genes in MHV-infected cells treated with 100 μM AEBSF as previously
280 described. As anticipated, *calreticulin* and *Grp94* transcription was greatly reduced in AEBSF-
281 treated cells (S5F Figure).
282
283 Having shown these compounds effectively inhibit the UPR in the context of infection, we
284 moved on to assess whether this could lead to an inhibition of viral replication. Cells were
285 infected with MHV at MOI 5 and treated with the UPRi. At 8 h p.i., tissue culture supernatant
286 was harvested and released progeny quantified by plaque assay. We found significant
287 reductions in virus titres for all UPRi treatments in comparison to control cells, with fold
288 reductions of between ~two-fold (IREi) and ~six-fold (ISRIB) (Fig 3A). This supports our
289 hypothesis that modulation of the UPR can have antiviral effects.
290
291 Next, we investigated whether using the UPRi in combination would have a cumulative effect
292 on virus release. We confirmed that combination treatment conditions led to reversal of the
293 three branches of the UPR, assayed as described above (S6 Figure). Fig 3B shows virus titres
294 from infected cells (8 h p.i.) at MOI 1 (blue) and MOI 5 (red), treated with different UPRi
295 combinations. Reductions in virus titre ranged from ~four-fold, in cells incubated with PERKi
296 and ISRIB (both targeting the PERK-eIF2α-ATF4 branch), to ~40- and ~100-fold (MOI 5 and
297 1 respectively), in cells treated with IREi and AEBSF (targeting the IRE1α and the ATF6
298 pathways). This was further confirmed by western blotting, demonstrating a striking decrease

299 in N protein levels for treatment combinations where virus titres were lowest (Fig 3C). In
300 addition, cell monolayers infected with MHV in the presence of IREi and AEBSF showed
301 delayed cytopathic effect, as indicated by reduced syncytium formation, likely due to lower
302 virus production (Fig 3D).
303
304 **Mechanistic analysis of the UPR activation by SARS-CoV-2 proteins**
305 Having established the use of UPRi as a potential antiviral strategy, we moved on to study UPR
306 activation by SARS-CoV-2, initially assaying the cellular response to individual virus proteins
307 in the context of transfection.
308
309 Previous studies have indicated that expression of the SARS-CoV spike (S) protein can activate
310 the PERK-eIF2α-ATF4 branch [47] whereas the MHV S protein activates the IRE1α-XBP1
311 pathway (28). In addition, SARS-CoV ORF3a and ORF8 were found to activate the PERK-
312 eIF2α-ATF4 and ATF6 pathways, respectively [48,49]. To define the UPR activation
313 associated with the counterpart proteins from SARS-CoV-2, we expressed C-terminally-tagged
314 S (S-HA), ORF3a (ORF3a-FLAG) and ORF8 (ORF8-FLAG) proteins in human embryonic
315 kidney cells (HEK-293T cells). N, a structural protein which is not documented as activating
316 the UPR, was over-expressed as a negative control (N-FLAG).
317
318 ER stress, assessed by the induction of HERP and BiP, was induced by SARS-CoV-2 S but not
319 N (S7A Figure). The PERK-eIF2α-ATF4 branch was activated from 24 h p.t. onwards, as
320 indicated by the phosphorylation of eIF2α and the detection of ATF4 (S7A Figure), although
321 phosphorylation of PERK was not clearly evident. The activation of this pathway was further
322 confirmed by the increase in *CHOP* transcription compared to mock-transfected cells (S7B
323 Figure). The amino terminus of ATF6 (ATF6-Nt) was detected in S-transfected cells from 24

324 h p.t. onwards (S7A Figure), indicating activation of the ATF6 branch. Activation of the IRE1α
325 pathway is also evident from an increase in the spliced form of *XBP1* in S protein-transfected
326 cells (S7A Figure). Contrary to previous findings for SARS-CoV, this indicates that the
327 expression of the SARS-CoV-2 S protein is sufficient to induce all three major signalling
328 pathways of the UPR.
329
330 In the case of SARS-CoV-2 ORF8 transfection, IRE1α-XBP1 and ATF6 were the main
331 pathways induced (S7C Figure), again contrasting with findings for SARS-CoV [49]. Although
332 a slight activation of ATF4 was observed in ORF8-transfected cells at 36 h p.t. (S7C Figure),
333 this was not accompanied by PERK nor eIF2a phosphorylation, and induction of *CHOP*
334 transcription was lower than in S protein-transfected cells (S7B Figure). SARS-CoV-2 ORF3a
335 transfection did not induce any of the branches of the UPR (S7C Figure).
336
337 We then asked whether the UPR induction caused by SARS-CoV-2 S and ORF8
338 overexpression could be reversed by treatment with UPRi. This was confirmed for each
339 inhibitor individually (S8 Figure). Additionally, we tested this using a combination treatment
340 condition (Fig 4), for which we selected IREi/AEBSF as this gave the most promising reduction
341 in viral titre during MHV infection (Fig 3B). Treatment of SARS-CoV-2 S- and ORF8-
342 transfected cells with IREi/AEBSF reduced expression of HERP and BiP to levels comparable
343 to mock-transfected cells (Fig 4A, 36 h p.t.). This indicates the treatment successfully reversed
344 the UPR activation by the two viral proteins. PERK pathway inhibition was evident in treated
345 cells from the reduction in PERK and eIF2α phosphorylation (Fig 4A); however, ATF4 levels
346 appeared to be slightly increased under these conditions, as was induction of its target gene
347 *CHOP* (S8C Figure). ATF4 induction in the presence of IREi has been previously described

348 [50]. Inhibition of the ATF6 and the IRE1α-XBP1 pathways was also evident, as very little
349 ATF6-Nt and *XBP1-s* were present in IREi/AEBSF treated cells (Fig 4A and Fig 4B).
350
351 In summary, over-expression of the S and the ORF8 proteins of SARS-CoV-2 is sufficient to
352 activate the three branches of the UPR, and this can be reversed by UPRi treatment.
353
354 **Induction of the UPR in SARS-CoV-2-infected cells**
355 We went on to study UPR activation in the context of SARS-CoV-2 infection. Vero CCL81
356 cells were infected at MOI 1 and harvested at 24 and 48 h p.i. Lysates were analysed as above.
357 As shown in Fig 5A, the PERK-eIF2α-ATF4 branch was activated as indicated by increased
358 phosphorylation of PERK and eIF2α. This was further confirmed by the induction of ATF4
359 (Fig 5A) and *CHOP* in infected cells (S9A Figure). Detection of ATF6-Nt (Fig 5A)
360 demonstrates that the ATF6 pathway is also activated during the course of infection. In
361 addition, activation of the IRE1α pathway was evident from an increase in the spliced form of
362 *XBP1* in SARS-CoV-2-infected cells at 48 h p.i. (Fig 5A). We conclude that SARS-CoV-2
363 infection induces all three branches of the UPR.
364
365 **Effect of the IREi/AEBSF combination on SARS-CoV-2 infection**
366 Next, we investigated whether the previously described UPRi combinations could also be used
367 as potential antiviral drugs against SARS-CoV-2. The gastrointestinal tract is known to be one
368 of the key sites of SARS-CoV-2 infection *in vivo* [51] so we used Caco2 cells, human intestinal
369 cells shown to be permissive for SARS-CoV-2 infection [52,53]. Cells were infected with
370 SARS-CoV-2 at MOI 0.01 and treated with the different UPRi combinations. Supernatants
371 were harvested at 48 h p.i. and released virions quantified by $TCID_{50}$ assay (Fig 5B).
372 Reductions in virus titre were observed and these were generally much greater than those seen

373 for MHV (MOI 1 and 5, Fig 3B), with both the PERKi/IREi and IREi/AEBSF combinations
374 reducing virus titres to below the limit of detection.
375
376 As the IREi/AEBSF combination had the greatest inhibitory activity against both MHV and
377 SARS-CoV-2, we tested whether this combination could inhibit SARS-CoV-2 infection at a
378 higher MOI. In addition to Vero CCL81 cells we employed a human lung cell line (Calu3) as
379 a model for the primary site of SARS-CoV-2 infection, the lung [52,53]. Cells were infected at
380 MOI 1 or MOI 5 and virus titres assessed by plaque assays at 24 h p.i. Incubation of Vero cells
381 with IREi/AEBSF led to a statistically significant (p = 0.0241 for MOI 1 and p = 0.0033 for
382 MOI 5) ~100-fold reduction in virus titre (Fig 5C, left). In Calu3 cells, IREi/AEBSF treatment
383 had an even greater antiviral effect, reducing released virions by ~1,000-fold (p = 0.0017) to at
384 or around the limit of detection (Fig 5C, right).
385
386 Detailed analysis of the activation of the three UPR pathways under the IREi/AEBSF treatment
387 condition was performed in SARS-CoV-2-infected Vero CCL81 cells at 24 and 48 h p.i. (Fig
388 5A and S9A Figure). Interestingly, in both SARS-CoV-2- and MHV-infected cells, the
389 IREi/AEBSF combination was not only able to prevent activation of the IREi and ATF6
390 pathways, but also the PERK-eIF2α-ATF4 branch, as indicated by reduced phosphorylation of
391 PERK and eIF2α (Fig 5A and S6 Figure) and reduced transcription of *Chop* (S6C Figure and
392 S9A Figure). This may be due to the inhibition of viral replication leading to a reduced ER
393 load, as opposed to specific inhibition of the PERK pathway. This is supported by the
394 observation of a striking decrease in viral protein levels in infected cells treated with
395 IREi/AEBSF (Fig 3C and Fig 5A), consistent with reduced viral replication. This reversal of
396 CoV-induced UPR activation by the UPRi suggests that the antiviral activity of these

397 compounds can be attributed, at least in part, to specific inhibition of the UPR, a pathway which
398 is evidently required for efficient viral replication.
399
400 In addition to its role in UPR inhibition, AEBSF has also been reported to inhibit TMPRSS2
401 [54,55], a host serine protease essential for SARS-CoV-2 cell entry [53]. To test whether
402 AEBSF treatment inhibits SARS-CoV-2 cell entry, we transfected HEK-293T cells with
403 TMPRSS2 and ACE2, the SARS-CoV-2 cell entry receptor [56] and incubated them with
404 lentiviral particles pseudotyped with the SARS-CoV-2 S protein (S9B Figure). No significant
405 inhibition of viral entry was observed upon treatment with 100μM AEBSF for 4 hours,
406 suggesting that the antiviral activity of AEBSF is predominantly due to its inhibition of the
407 UPR.
408
409 **Discussion**
410 This study reveals that all three branches of the UPR are activated upon MHV and SARS-CoV-
411 2 infection, and highlights this as a very prominent pathway in the host response. The UPR was
412 the most significantly enriched Reactome pathway associated with genes transcriptionally up-
413 regulated during MHV infection and, consistent with previous studies, we show activation of
414 all three branches of the UPR by MHV [26,28]. Confirming the importance of this in SARS-
415 CoV-2 infection, ER-related GO/KEGG terms are enriched in the differentially expressed
416 genes lists of several proteomics/transcriptomics studies on SARS-CoV-2-infected cells
417 [30,57–60]. This is also a very prominent theme in proteomics studies identifying host
418 interaction partners of SARS-CoV-2 proteins, in which ER proteins are reproducibly found
419 [59,61,62]. In one such study, "response to endoplasmic reticulum stress" was the most highly
420 enriched biological process GO annotation associated with the host interaction partners [62].
421 This suggests that SARS-CoV-2, like other CoVs [63–65], enacts a finely tuned modulation of

422 the UPR that may involve direct interactions with its components. Despite this, the activation
423 of the three branches of the UPR by SARS-CoV-2 has not been previously described, although
424 it has been characterised for other CoVs [4,30,63,66–70] including the closely related SARS-
425 CoV [28,47–49,71–75]. Here we show that, like MHV, SARS-CoV-2 infection induces all
426 three branches of the UPR, in contrast to results from SARS-CoV infection, in which only the
427 PERK branch was activated [28,71,72].
428
429 Over-expression of the individual SARS-CoV-2 S or ORF8 proteins initiates UPR signalling.
430 S protein was found to induce all three branches of the UPR in contrast to the counterpart
431 protein of SARS-CoV, which appears to induce exclusively the PERK pathway [47]. Similarly,
432 we identify ORF8 of SARS-CoV-2 as an inducer of both the IRE1α and ATF6 branches of the
433 UPR, whereas the SARS-CoV equivalent has been shown to activate only ATF6 [49]. These
434 differences can partly be explained by sequence divergence between the two viruses [76].
435 SARS-CoV-2 ORF8, for example, lacks the VLVVL motif that causes SARS-CoV ORF8
436 (specifically ORF8b) to aggregate and trigger intracellular stress pathways [74]. Furthermore,
437 SARS-CoV ORF8ab was shown to mediate activation of the ATF6 pathway through a direct
438 interaction with the ATF6 ER-lumenal domain [49], although it is undetermined whether the
439 corresponding interaction occurs with SARS-CoV-2 ORF8. Recent proteomics-based
440 interactome studies have identified interactions between SARS-CoV-2 ORF8 and several ER
441 quality control proteins [59,61], which could contribute to the ORF8-induced UPR induction
442 observed in our study. Alterations to this key UPR modulator have important ramifications:
443 mutation or deletion of ORF8 in naturally occurring strains of SARS-CoV and SARS-CoV-2
444 correlate with milder disease and, in the latter case, lower incidence of hypoxia [77–80].
445

446 Here, we also demonstrate the importance of UPR activation to CoV infection by showing that
447 pharmacological inhibition of the UPR leads to significant reductions in titres of virions
448 released from MHV- and SARS-CoV-2-infected cells. Simultaneous inhibition of the IRE1α
449 and ATF6 pathways by STF-083010 and AEBSF respectively, was particularly effective,
450 reducing virus titres by up to ~1,000-fold. These drugs have been extensively used in
451 preclinical studies for neurodegenerative diseases, cancer and pulmonary fibrosis [45,81–85].
452 Thus the STF-083010/AEBSF combination is a promising antiviral candidate to rapidly
453 progress into a clinical trial.
454
455 To date, the development of antivirals against SARS-CoV-2 has focused on drugs targeting
456 virus replication, such as remdesivir. However, these antiviral therapies do not take into
457 account that the pathophysiology associated with COVID-19 is mostly related to an aberrant
458 cellular response. In some clinical manifestations of COVID-19, an exacerbated UPR could
459 play a key role [86–88]. For example, activation of ER stress and the UPR is one of the major
460 triggers of endothelial dysfunction [89,90], which is associated with acute respiratory distress
461 syndrome (ARDS) [91], a diffuse inflammatory lung injury present in 20-67% of hospitalised
462 patients [92,93]. Other clinical manifestations of COVID-19 such as thromboembolism,
463 cerebro- and cardiovascular diseases and neurological complications, are also associated with
464 endothelial dysfunction [94]. Furthermore, a recognised sequela of COVID-19 is pulmonary
465 fibrosis [95], which can develop in up to 17% of COVID-19 patients [96]. Pulmonary fibrosis
466 is a severe form of interstitial lung disease characterised by progressive dyspnea, hypoxemia,
467 and respiratory failure due to the presence of patchy areas of fibrotic tissue. ER stress and UPR
468 activation are known to be involved in the development and progression of this fibrotic disease
469 [97]. This suggests that UPR activation in response to SARS-CoV-2 infection contributes to
470 the lung pathophysiology associated with COVID-19. Therefore, the UPR inhibitors used in

471 this study could have a dual therapeutic effect, not only contributing to the reduction of viral
472 burden in patients, but also diminishing the pathophysiology associated with COVID-19. In
473 addition, the idea of targeting an exaggerated cellular response instead of the virus itself
474 substantially reduces the chances of generating virus escape mutants.
475
476 **Materials and Methods**
477
478 **Cells and viruses:** Murine 17 clone 1 (17 Cl-1), Calu3 (ATCC, HTB-55) and Vero (ATCC,
479 CCL81) cells were maintained in Dulbecco's modification of Eagle's medium supplemented
480 with 10% (vol/vol) fetal calf serum (FCS). HEK-293T cells (ATCC, CRL-11268) were
481 cultured in DMEM supplemented with 5% FCS. Caco2 cells were a kind gift from Dr Valeria
482 Lulla and were maintained in DMEM supplemented with 20% FCS. All cell lines were cultured
483 in medium containing 100 U/ml penicillin, 100 µg/ml streptomycin and 1 mM L-glutamine.
484 Cells were incubated at 37 °C in the presence of 5% CO_2.
485 Recombinant MHV strain A59 (MHV-A59) was derived as described previously [98]. Upon
486 reaching 70–80% confluence, 17 Cl-1 cells were infected with MHV-A59 at MOI 5 as
487 described(99,100). Vero CCL81 and Calu3 cells were infected with SARS-CoV-2 (SARS-
488 CoV-2/human/Switzerland/ZH-UZH-IMV5/2020) at two MOIs (1 and 5) for 24 or 48 h as
489 previously described [99,100]. Caco2 cells were infected with SARS-CoV-2 (isolate hCoV-
490 19/Edinburgh/2/2020, a kind gift from Dr Christine Tait-Burkhard and Dr Juergen Haas) at
491 MOI 0.01 and incubated for 48 h in MEM containing 1% L-glutamine, 1% non-essential
492 aminoacids, 1% penicillin/streptomycin and supplemented with 2% FBS.
493
494 **Ribosomal profiling and RNASeq data:** 17 Cl-1 cells were grown on 100-mm dishes to 90%
495 confluency and infected with MHV-A59 at MOI 10. At the indicated time-points, cells were

496 rinsed with 5 ml of ice-cold PBS, flash frozen in a dry ice/ethanol bath and lysed with 400 µl
497 of lysis buffer [20 mM Tris-HCl pH 7.5, 150 mM NaCl, 5 mM $MgCl_2$, 1 mM DTT, 1% Triton
498 X-100, 100 µg/ml cycloheximide and 25 U/ml TURBO DNase (Life Technologies)]. The cells
499 were scraped extensively to ensure lysis, collected and triturated ten times with a 26-G needle.
500 Cell lysates were clarified by centrifugation at 13,000 *g* for 20 min at 4 °C. Lysates were
501 subjected to RiboSeq and RNASeq based on previously reported protocols [7,101]. Ribosomal
502 RNA was removed using Ribo-Zero Gold rRNA removal kit (Illumina) and library amplicons
503 were constructed using a small RNA cloning strategy adapted to Illumina smallRNA v2 to
504 allow multiplexing. Amplicon libraries were deep sequenced using an Illumina NextSeq500
505 platform. Due to the very large amounts of vRNA produced during infection, mock samples
506 were processed separately from infected samples to avoid contamination. RiboSeq and
507 RNASeq sequencing data have been deposited in the ArrayExpress database
508 (http://www.ebi.ac.uk/arrayexpress) under the accession numbers E-MTAB-8650 and E-
509 MTAB-8651.
510
511 **Computational analysis of RiboSeq and RNASeq data:** Reads were trimmed for adaptor
512 sequences, filtered for length ≥ 25 nt, and reads mapping to *Mus musculus* rRNA (downloaded
513 from the SILVA database [102] or MHV-A59 viral RNA (GenBank accession AY700211.1)
514 (with up to 2 mismatches) removed, as previously described [7]. The remaining reads were
515 aligned directly to the mouse genome (FASTA and GTF gencode release M20, GRCm38,
516 primary assembly) (with up to 2 mismatches) using STAR (parameters: --outFilterIntronMotifs
517 RemoveNoncanonicalUnannotated --outMultimapperOrder Random) [103]. Reads on protein-
518 coding genes were tabulated using htseq-count (version 0.9.1), covering the whole gene for
519 differential transcription analysis (parameters: -a 0 -m union -s yes -t gene) and just the CDS

520 for the translation efficiency analysis (parameters: -a 0 -m intersection-strict -s yes -t CDS)
521 [104], using the GTF file from the above Gencode release as the gene feature annotation.
522
523 Differential transcription analysis was performed using DESeq2 (version 1.18.1) [8] and
524 translation efficiency analysis with Xtail (version 1.1.5) [10]. For each analysis, low count
525 genes (with fewer than ten counts from all samples combined) were discarded, following which
526 read counts were normalised by the total number of reads mapping to host mRNA for that
527 library, using standard DESeq2 normalisation. This minimises the effect of the large amount
528 of vRNA present in infected samples. Shrinkage of the transcriptional fold changes to reduce
529 noise in lowly-expressed genes was applied using lfcShrink (parameter: type='normal').
530
531 A given gene was considered to be differentially expressed if the FDR-corrected *p* value was
532 less than 0.05 and the fold change between the means of infected and mock replicates was
533 greater than two. Volcano plots and transcription versus TE comparison plots were generated
534 using R and FDR-corrected *p* values and $\log_2$(fold change) values from the DESeq2 and Xtail
535 analyses. All reported *p* values are corrected for multiple testing by the Benjamini-Hochberg
536 method. Fold changes plotted in the transcription vs TE comparison are not filtered for
537 significant *p* values before plotting.
538
539 To plot RNASeq and RPF profiles for specific transcripts, reads were mapped to the specified
540 transcript from the NCBI genome assembly using bowtie [105] allowing two mismatches
541 (parameters: -v 2, --best). Coordinates for known uORFs were taken from the literature
542 [11,12,23] and the positions of start and stop codons in all frames determined. Read density
543 (normalised by total reads mapping to host mRNA for each library, to give reads per million
544 mapped reads) was calculated at each nucleotide on the transcript and plotted, coloured

545 according to phase. Read positions were offset by +12 nt so that plotted data represent the
546 inferred position of the ribosomal P site. Bar widths were increased to 12 nt (Fig 1E) or 4 nt
547 (Supplementary Fig 2) to aid visibility and were plotted sequentially starting from the 5′ end
548 of the transcript.
549
550 **Gene ontology and Reactome pathway enrichment analyses:** Lists of gene IDs of
551 significantly differentially expressed genes (Supplementary Table 2) were used for GO term
552 enrichment analysis by the PANTHER web server under the default conditions (release
553 20190606, GO database released 2019-02-02) [106], against a background list of all the genes
554 that passed the threshold for inclusion in that expression analysis. For Reactome pathway
555 enrichment (version 69) [9], the same differentially expressed gene lists were converted to their
556 human orthologues and analysed, both using the reactome.org web server to determine which
557 pathways are significantly over-represented (FDR-corrected p value ≤ 0.05).
558
559 **Enrichment analysis for eIF2α-phosphorylation-resistant genes:**
560 Resistance to translational repression by p-eIF2α is not an existing GO term, so a list of genes
561 reported to be p-eIF2α-resistant was constructed based on Andreev et al., 2015 [16] and
562 references within (excluding those from IRESite, which were not found to be p-eIF2α-resistant
563 in their study). Mouse homologues of these genes were identified using the NCBI homologene
564 database (Supplementary Table 4). Enrichment of genes categorised as p-eIF2α-resistant
565 amongst the genes with significantly increased translational efficiency, compared to a
566 background of all *Mus musculus* genes included in the TE analysis with any GO annotation,
567 was calculated using a Fisher Exact test.
568

569 **Chemicals:** GSK-2606414 was a kind gift from Dr Edward Emmott and Prof Ian Goodfellow.
570 AEBSF, STF-083010, ISRIB and tunicamycin were purchased from Sigma-Aldrich. GSK-
571 2606414, STF-083010, ISRIB and tunicamycin were dissolved in DMSO, whereas AEBSF
572 was dissolved in water, to the required concentrations. In all experiments, the final
573 concentration of DMSO did not exceed 0.4%. Cytotoxicity after treatment with single and
574 combined UPR inhibitors was measured using the Cell Titer Blue (Promega) and trypan blue
575 exclusion kits (Sigma), following manufacturer's instructions.
576
577 **Antibodies:** The following primary antibodies were used: mouse monoclonal antibodies
578 against MHV N and S proteins (kind gifts of Dr Helmut Wege, University of Würzburg), mouse
579 anti-GAPDH (IgM specific, G8795, Sigma-Aldrich), mouse anti-Flag (F3165, Sigma-Aldrich),
580 rabbit anti-HA (3724, Cell Signaling Technology), rabbit anti-PERK (ab229912, Abcam),
581 rabbit anti-HERPUD1 (ab150424, Abcam), rabbit anti-GRP78 (BIP, ab108613, Abcam), rabbit
582 anti-eIF2α (9722, Cell Signaling Technology), rabbit anti-phospho-eIF2α (Ser51, 9721, Cell
583 Signaling Technology), rabbit anti-ATF4 (10835-1-AP, Proteintech), rabbit anti-ATF6
584 (ab203119 and ab37149, Abcam), mouse anti-S6 (2317, Cell Signaling Technology) and rabbit
585 RPL10a (ab174318, Abcam). Secondary antibodies used for western blotting were purchased
586 from Licor: IRDye 800CW Donkey Anti-Mouse IgG (H+L), IRDye 800CW Donkey Anti-
587 Rabbit IgG (H+L), IRDye 680RD Goat Anti-Mouse IgG (H+L) and IRDye 680RD Goat Anti-
588 Mouse IgM (μ chain specific).
589
590 **Plasmids and transfections:** HEK-293T cells were transiently transfected with pcDNA3.1-
591 SARS-CoV-2-S-HA (kind gift of Dr Jerome Cattin and Prof Sean Munro, MRC-LMB,
592 Cambridge, UK), pcDNA6-SARS-CoV-2-N-FLAG, pcDNA6-SARS-CoV-2-ORF3a-FLAG
593 and pcDNA6-SARS-CoV-2-ORF8-FLAG plasmids (kind gifts of Prof Peihui Wang, Shandong

594 University, China) using a commercial liposome method (TransIT-LT1, Mirus). Transfection
595 mixtures containing plasmid DNA, serum-free medium (Opti-MEM; Gibco-BRL) and
596 liposomes were set up as recommended by the manufacturer and added dropwise to the tissue
597 culture growth medium. Cells were harvested at 24 and 36 h post-transfection.
598
599 **Immunoblotting:** Cells were lysed in 1X Laemmli's sample buffer. After denaturation at 98
600 ºC for 5 minutes, proteins were separated by 12% SDS-PAGE and transferred to nitrocellulose
601 membranes. These were blocked (5% non-fat milk powder or bovine serum albumin in PBST
602 [137 mM NaCl, 2.7 mM KCl, 10 mM Na_2HPO_4, 1.5 mM KH_2PO_4, pH 6.7, and 0.1% Tween
603 20]) for 30 min at room temparature and probed with specific primary antibodies at 4ºC
604 overnight. Membranes were incubated in the dark with IRDye-conjugated secondary
605 antibodies diluted to the recommended concentrations in PBST for 1 h at room temperature.
606 Blots were scanned using an Odyssey Infrared Imaging System (Licor).
607
608 **Analysis of *Xbp1* splicing by RT-PCR:** Total RNA was isolated from infected or transfected
609 cells as described previously [7], and cDNA synthesised from 500 ng total RNA using M-MLV
610 Reverse Transcriptase (Promega). Mouse or human *Xbp1* and *Rpl19* were amplified using
611 specific primers (Supplementary Table 5). Following PCR reactions, the resulting amplicons
612 were subjected to electrophoresis in 3% agarose gels.
613
614 **Quantitative real-time PCR assays:** Relative levels of mouse or human *Bip*, *Chop*, *Gadd34,*
615 *Calreticulin* and *Grp94* in cDNA samples were determined by quantitative real-time PCR
616 (qPCR) using a Rotor-Gene 3000 (Corbett Research). Reactions were performed in a final
617 volume of 20 µl containing Hot Start Taq (1 U, QIAGEN), 3.5 mM $MgCl_2$, 2.5 mM
618 deoxynucleotides, 450 nM SYBR Green dye, 500 nM relevant forward and reverse primers

619 (Supplementary Table 5) and 1 µl of cDNA. No-template controls were included for each
620 primer pair, and each qPCR reaction was carried out in duplicate. Fold changes in gene
621 expression relative to the mock were calculated by the delta delta-cycle threshold (ΔΔCt)
622 method, and *Rpl19* was used as a normalising housekeeping gene.
623
624 **Polysome profiling:** 17 Cl-1 cells were infected as described above. 10 min prior to harvesting,
625 cells were treated with cycloheximide (100 µg/ml), washed with PBS and lysed in a buffer
626 containing 20 mM Tris HCl pH 7.5, 100 mM KCl, 5 mM MgOAc, 0.375 mM CHX, 1 mM
627 DTT, 0.1 mM PMSF, 2 U/µl DNase I, 0.5% NP-40, supplemented with protease and
628 phosphatase inhibitors (ThermoFisher Scientific). Following trituration with a 26-G needle (ten
629 passes), lysates were cleared (13,000 *g* at 4 ºC for 20 min) and the supernatants layered onto
630 12 ml sucrose density gradients (10–50% sucrose in TMK buffer: 20 mM Tris-HCl pH 7.5,
631 100 mM KCl, 5 mM $MgCl_2$) prepared in Beckman SW41 polypropylene tubes using a Gradient
632 Master (Biocomp). Following centrifugation (200,000 *g* for 90 min at 4 ºC), fractions were
633 prepared using an ISCO fractionator monitoring absorbance at 254 nm. Proteins were
634 concentrated from fractions using methanol-chloroform extraction and subjected to
635 immunoblotting analysis. Polysome profiling in higher salt conditions was carried out as
636 described above except that the lysis buffer and sucrose density gradient contained 400 mM
637 KCl.
638
639 **Virus plaque assays:** To determine MHV-A59 titres by plaque assay, 17 Cl-1 cells in 6-well
640 plates were infected with 400 µl of 10-fold serial dilutions of sample in infection medium
641 (Hank's balanced salt solution containing 50 µg/ml DEAE-dextran and 0.2% bovine serum
642 albumin - BSA). After 45 min at 37°C with regular rocking, the inoculum was removed and
643 replaced with a 1:1 mixture of 2.4% Avicel and MEM 2X medium (20% MEM 10X, 2% non-

644 essential aminoacids, 200 U/ml penicillin, 200 µg/ml streptomycin, 2 mM L-glutamine, 40 mM
645 HEPES pH 6.8, 10% tryptose phosphate broth, 10% FCS and 0.01% sodium bicarbonate).
646 Plates were incubated at 37 ºC for 48 h prior to fixing with 3.7% formaldehyde in PBS. Cell
647 monolayers were stained with 0.1% toluidine blue to visualise plaques. SARS-CoV-2 plaque
648 assays were performed as previously described [99]). Experiments were conducted using three
649 biological repeats.
650
651 **$TCID_{50}$ assays:** SARS-CoV-2 replication was assessed using a 50% tissue culture infective
652 dose ($TCID_{50}$) assay in Vero E6 cells. Supernatant derived from infected Caco2 cells was
653 subjected to 10-fold serial dilutions. At 72 h p.i., cells were fixed and stained as previously
654 indicated. Wells showing any sign of cytopathic effect (CPE) were scored as positive.
655
656 **Statistical analysis of virus titre results:** Data were analysed in GraphPad Prism 9.0
657 (GraphPad software, San Diego, CA, USA). Values represent mean ± standard deviation.
658 Statistical significance was evaluated using two-tailed *t*-tests on $\log_{10}$(virus titre) data, which
659 did not assume equal variances for the two populations being compared, to calculate the *p*-
660 values. Differences as compared to the control with p value ≤ 0.05 were considered as
661 statistically significant, with *$p < 0.05$, ** $p < 0.01$, *** $p < 0.001$ and **** $p < 0.0001$.
662
663 **Acknowledgements**
664 SK, ND, GD and EB would like to acknowledge Dr Holly Shelton, Dr Isabelle Dietrich and Dr
665 Christine Reitmayer for their supervision in the CL3 suite, and Dr Christine Tait-Burkhard and
666 Dr Juergen Haas for the SARS-CoV-2 isolate.
667
668 NI would like to thank Dr James Edgar for providing SARS-CoV-2 plasmids.

NI would like to thank Dr Luke Meredith and Prof Ian Goodfellow for providing pcDNA3.1-ACE2, pcDNA3.1-TMPRSS2, pMD2-VSV-G and pNL4.3-Luc plasmids for pseudotyped virions.

References

1. Channappanavar R, Perlman S. Pathogenic human coronavirus infections: causes and consequences of cytokine storm and immunopathology. Seminars in Immunopathology. 2017 Jul 2;39(5).
2. Zhou P, Yang X-L, Wang X-G, Hu B, Zhang L, Zhang W, et al. A pneumonia outbreak associated with a new coronavirus of probable bat origin. Nature. 2020 Mar 12;579(7798).
3. Zhu N, Zhang D, Wang W, Li X, Yang B, Song J, et al. A Novel Coronavirus from Patients with Pneumonia in China, 2019. New England Journal of Medicine. 2020 Feb 20;382(8).
4. Fung TS, Liu DX. Coronavirus infection, ER stress, apoptosis and innate immunity. Frontiers in Microbiology. 2014 Jun 17;5.
5. Ron D, Walter P. Signal integration in the endoplasmic reticulum unfolded protein response. Nature Reviews Molecular Cell Biology. 2007 Jul;8(7).
6. Ingolia NT, Ghaemmaghami S, Newman JRS, Weissman JS. Genome-Wide Analysis in Vivo of Translation with Nucleotide Resolution Using Ribosome Profiling. Science. 2009 Apr 10;324(5924).
7. Irigoyen N, Firth AE, Jones JD, Chung BY-W, Siddell SG, Brierley I. High-Resolution Analysis of Coronavirus Gene Expression by RNA Sequencing and Ribosome Profiling. PLOS Pathogens. 2016 Feb 26;12(2).
8. Love MI, Huber W, Anders S. Moderated estimation of fold change and dispersion for RNA-seq data with DESeq2. Genome Biology. 2014 Dec 5;15(12).
9. Fabregat A, Sidiropoulos K, Viteri G, Forner O, Marin-Garcia P, Arnau V, et al. Reactome pathway analysis: a high-performance in-memory approach. BMC Bioinformatics. 2017 Dec 2;18(1).
10. Xiao Z, Zou Q, Liu Y, Yang X. Genome-wide assessment of differential translations with ribosome profiling data. Nature Communications. 2016 Sep 4;7(1).
11. Lu PD, Harding HP, Ron D. Translation reinitiation at alternative open reading frames regulates gene expression in an integrated stress response. Journal of Cell Biology. 2004 Oct 11;167(1).
12. Vattem KM, Wek RC. Reinitiation involving upstream ORFs regulates ATF4 mRNA translation in mammalian cells. Proceedings of the National Academy of Sciences. 2004 Aug 3;101(31).
13. Watatani Y, Ichikawa K, Nakanishi N, Fujimoto M, Takeda H, Kimura N, et al. Stress-induced Translation of ATF5 mRNA Is Regulated by the 5′-Untranslated Region. Journal of Biological Chemistry. 2008 Feb 1;283(5).
14. Zhou D, Palam LR, Jiang L, Narasimhan J, Staschke KA, Wek RC. Phosphorylation of eIF2 Directs *ATF5* Translational Control in Response to Diverse Stress Conditions. Journal of Biological Chemistry. 2008 Mar 14;283(11).
15. Palam LR, Baird TD, Wek RC. Phosphorylation of eIF2 Facilitates Ribosomal Bypass of an Inhibitory Upstream ORF to Enhance *CHOP* Translation. Journal of Biological Chemistry. 2011 Apr 1;286(13).
16. Andreev DE, O'Connor PB, Fahey C, Kenny EM, Terenin IM, Dmitriev SE, et al. Translation of 5′ leaders is pervasive in genes resistant to eIF2 repression. eLife. 2015 Jan 26;4.
17. Brush MH, Weiser DC, Shenolikar S. Growth Arrest and DNA Damage-Inducible Protein GADD34 Targets Protein Phosphatase 1α to the Endoplasmic Reticulum and Promotes

717 Dephosphorylation of the α Subunit of Eukaryotic Translation Initiation Factor 2. Molecular and
718 Cellular Biology. 2003 Feb 15;23(4).
719 18. Novoa I, Zeng H, Harding HP, Ron D. Feedback Inhibition of the Unfolded Protein Response
720 by GADD34-Mediated Dephosphorylation of eIF2α. Journal of Cell Biology. 2001 May
721 28;153(5).
722 19. Lee Y-Y, Cevallos RC, Jan E. An Upstream Open Reading Frame Regulates Translation of
723 GADD34 during Cellular Stresses That Induce eIF2α Phosphorylation. Journal of Biological
724 Chemistry. 2009 Mar 13;284(11).
725 20. Mungrue IN, Pagnon J, Kohannim O, Gargalovic PS, Lusis AJ. CHAC1/MGC4504 Is a Novel
726 Proapoptotic Component of the Unfolded Protein Response, Downstream of the ATF4-ATF3-
727 CHOP Cascade. The Journal of Immunology. 2009 Jan 1;182(1).
728 21. Yamamoto K. Differential Contributions of ATF6 and XBP1 to the Activation of Endoplasmic
729 Reticulum Stress-Responsive cis-Acting Elements ERSE, UPRE and ERSE-II. Journal of
730 Biochemistry. 2004 Sep 1;136(3).
731 22. Baumeister P, Luo S, Skarnes WC, Sui G, Seto E, Shi Y, et al. Endoplasmic Reticulum Stress
732 Induction of the Grp78/BiP Promoter: Activating Mechanisms Mediated by YY1 and Its
733 Interactive Chromatin Modifiers. Molecular and Cellular Biology. 2005 Jun 1;25(11).
734 23. Yoshida H, Matsui T, Yamamoto A, Okada T, Mori K. XBP1 mRNA Is Induced by ATF6 and
735 Spliced by IRE1 in Response to ER Stress to Produce a Highly Active Transcription Factor.
736 Cell. 2001 Dec;107(7).
737 24. Nishitoh H. CHOP is a multifunctional transcription factor in the ER stress response. Journal
738 of Biochemistry. 2012 Mar 1;151(3).
739 25. Ma Y, Hendershot LM. Delineation of a Negative Feedback Regulatory Loop That Controls
740 Protein Translation during Endoplasmic Reticulum Stress. Journal of Biological Chemistry.
741 2003 Sep 12;278(37).
742 26. Bechill J, Chen Z, Brewer JW, Baker SC. Coronavirus Infection Modulates the Unfolded
743 Protein Response and Mediates Sustained Translational Repression. Journal of Virology. 2008
744 May 1;82(9).
745 27. Jiang X-S, Tang L-Y, Dai J, Zhou H, Li S-J, Xia Q-C, et al. Quantitative Analysis of Severe
746 Acute Respiratory Syndrome (SARS)-associated Coronavirus-infected Cells Using Proteomic
747 Approaches. Molecular & Cellular Proteomics. 2005 Jul;4(7).
748 28. Versteeg GA, van de Nes PS, Bredenbeek PJ, Spaan WJM. The Coronavirus Spike Protein
749 Induces Endoplasmic Reticulum Stress and Upregulation of Intracellular Chemokine mRNA
750 Concentrations. Journal of Virology. 2007 Oct 15;81(20).
751 29. Yeung Y-S, Yip C-W, Hon C-C, Chow KYC, Ma ICM, Zeng F, et al. Transcriptional profiling
752 of Vero E6 cells over-expressing SARS-CoV S2 subunit: Insights on viral regulation of
753 apoptosis and proliferation. Virology. 2008 Feb;371(1).
754 30. Shaban MS, Müller C, Mayr-Buro C, Weiser H, Albert BV, Weber A, et al. Inhibiting
755 coronavirus replication in cultured cells by chemical ER stress. bioRxiv [Preprint]. 2020.
756 Available from: https://www.biorxiv.org/content/10.1101/2020.08.26.266304v1.full
757 31. Harding HP, Zhang Y, Ron D. Protein translation and folding are coupled by an endoplasmic-
758 reticulum-resident kinase. Nature. 1999 Jan 21;397(6716).
759 32. Harding HP, Zhang Y, Bertolotti A, Zeng H, Ron D. Perk Is Essential for Translational
760 Regulation and Cell Survival during the Unfolded Protein Response. Molecular Cell. 2000
761 May;5(5).
762 33. Lu PD, Harding HP, Ron D. Translation reinitiation at alternative open reading frames regulates
763 gene expression in an integrated stress response. Journal of Cell Biology. 2004 Oct 11;167(1).
764 34. Harding HP, Novoa I, Zhang Y, Zeng H, Wek R, Schapira M, et al. Regulated Translation
765 Initiation Controls Stress-Induced Gene Expression in Mammalian Cells. Molecular Cell. 2000
766 Nov;6(5).
767 35. Calfon M, Zeng H, Urano F, Till JH, Hubbard SR, Harding HP, et al. IRE1 couples endoplasmic
768 reticulum load to secretory capacity by processing the XBP-1 mRNA. Nature. 2002 Jan
769 3;415(6867).

36. Ye J, Rawson RB, Komuro R, Chen X, Davé UP, Prywes R, et al. ER Stress Induces Cleavage of Membrane-Bound ATF6 by the Same Proteases that Process SREBPs. Molecular Cell. 2000 Dec;6(6).
37. Haze K, Yoshida H, Yanagi H, Yura T, Mori K. Mammalian Transcription Factor ATF6 Is Synthesized as a Transmembrane Protein and Activated by Proteolysis in Response to Endoplasmic Reticulum Stress. Molecular Biology of the Cell. 1999 Nov;10(11).
38. Bommiasamy H, Back SH, Fagone P, Lee K, Meshinchi S, Vink E, et al. ATF6 induces XBP1-independent expansion of the endoplasmic reticulum. Journal of Cell Science. 2009 May 15;122(10).
39. Lee A-H, Iwakoshi NN, Glimcher LH. XBP-1 Regulates a Subset of Endoplasmic Reticulum Resident Chaperone Genes in the Unfolded Protein Response. Molecular and Cellular Biology. 2003 Nov 1;23(21).
40. Luo S, Baumeister P, Yang S, Abcouwer SF, Lee AS. Induction of Grp78/BiP by Translational Block. Journal of Biological Chemistry. 2003 Sep 26;278(39).
41. Gao P, Chai Y, Song J, Liu T, Chen P, Zhou L, et al. Reprogramming the unfolded protein response for replication by porcine reproductive and respiratory syndrome virus. PLOS Pathogens. 2019 Nov 18;15(11).
42. Axten JM, Medina JR, Feng Y, Shu A, Romeril SP, Grant SW, et al. Discovery of 7-Methyl-5-(1-{[3-(trifluoromethyl)phenyl]acetyl}-2,3-dihydro-1 *H* -indol-5-yl)-7 *H* -pyrrolo[2,3- *d*]pyrimidin-4-amine (GSK2606414), a Potent and Selective First-in-Class Inhibitor of Protein Kinase R (PKR)-like Endoplasmic Reticulum Kinase (PERK). Journal of Medicinal Chemistry. 2012 Aug 23;55(16).
43. Harding HP, Zyryanova AF, Ron D. Uncoupling Proteostasis and Development *in Vitro* with a Small Molecule Inhibitor of the Pancreatic Endoplasmic Reticulum Kinase, PERK. Journal of Biological Chemistry. 2012 Dec 28;287(53).
44. Zyryanova AF, Kashiwagi K, Rato C, Harding HP, Crespillo-Casado A, Perera LA, et al. ISRIB Blunts the Integrated Stress Response by Allosterically Antagonising the Inhibitory Effect of Phosphorylated eIF2 on eIF2B. Molecular Cell. 2020 Nov;
45. Papandreou I, Denko NC, Olson M, van Melckebeke H, Lust S, Tam A, et al. Identification of an Ire1alpha endonuclease specific inhibitor with cytotoxic activity against human multiple myeloma. Blood. 2011 Jan 27;117(4).
46. Okada T, Haze K, Nadanaka S, Yoshida H, Seidah NG, Hirano Y, et al. A Serine Protease Inhibitor Prevents Endoplasmic Reticulum Stress-induced Cleavage but Not Transport of the Membrane-bound Transcription Factor ATF6. Journal of Biological Chemistry. 2003 Aug 15;278(33).
47. Chan C-P, Siu K-L, Chin K-T, Yuen K-Y, Zheng B, Jin D-Y. Modulation of the Unfolded Protein Response by the Severe Acute Respiratory Syndrome Coronavirus Spike Protein. Journal of Virology. 2006 Sep 15;80(18).
48. Minakshi R, Padhan K, Rani M, Khan N, Ahmad F, Jameel S. The SARS Coronavirus 3a Protein Causes Endoplasmic Reticulum Stress and Induces Ligand-Independent Downregulation of the Type 1 Interferon Receptor. PLoS ONE. 2009 Dec 17;4(12).
49. Sung S-C, Chao C-Y, Jeng K-S, Yang J-Y, Lai MMC. The 8ab protein of SARS-CoV is a luminal ER membrane-associated protein and induces the activation of ATF6. Virology. 2009 May;387(2).
50. Barez SR, Atar AM, Aghaei M. Mechanism of inositol-requiring enzyme 1-alpha inhibition in endoplasmic reticulum stress and apoptosis in ovarian cancer cells. Journal of Cell Communication and Signaling. 2020 Dec 21;14(4).
51. Lamers MM, Beumer J, van der Vaart J, Knoops K, Puschhof J, Breugem TI, et al. SARS-CoV-2 productively infects human gut enterocytes. Science. 2020 Jul 3;369(6499).
52. Chu H, Chan JF-W, Yuen TT-T, Shuai H, Yuan S, Wang Y, et al. Comparative tropism, replication kinetics, and cell damage profiling of SARS-CoV-2 and SARS-CoV with implications for clinical manifestations, transmissibility, and laboratory studies of COVID-19: an observational study. The Lancet Microbe. 2020 May;1(1).

53. Hoffmann M, Kleine-Weber H, Schroeder S, Krüger N, Herrler T, Erichsen S, et al. SARS-CoV-2 Cell Entry Depends on ACE2 and TMPRSS2 and Is Blocked by a Clinically Proven Protease Inhibitor. Cell. 2020 Apr;181(2).
54. Azouz NP, Klingler AM, Rothenberg ME. Alpha 1 antirypsin is an inhibitor of the SARS-CoV-2 priming protease TMPRSS2. bioRxiv [Preprint]. 2020. Available from: https://www.biorxiv.org/content/10.1101/2020.05.04.077826v2
55. Shen LW, Mao HJ, Wu YL, Tanaka Y, Zhang W. TMPRSS2: A potential target for treatment of influenza virus and coronavirus infections. Biochimie. 2017 Nov;142.
56. Daly JL, Simonetti B, Klein K, Chen K-E, Williamson MK, Antón-Plágaro C, et al. Neuropilin-1 is a host factor for SARS-CoV-2 infection. Science. 2020 Nov 13;370(6518).
57. Grenga L, Gallais F, Pible O, Gaillard J-C, Gouveia D, Batina H, et al. Shotgun proteomics analysis of SARS-CoV-2-infected cells and how it can optimize whole viral particle antigen production for vaccines. Emerging Microbes & Infections. 2020 Jan 1;9(1).
58. Appelberg S, Gupta S, Svensson Akusjärvi S, Ambikan AT, Mikaeloff F, Saccon E, et al. Dysregulation in Akt/mTOR/HIF-1 signaling identified by proteo-transcriptomics of SARS-CoV-2 infected cells. Emerging Microbes & Infections. 2020 Jan 1;9(1).
59. Stukalov A, Girault V, Grass V, Bergant V, Karayel O, Urban C, et al. Multi-level proteomics reveals host-perturbation strategies of SARS-CoV-2 and SARS-CoV. bioRxiv [Preprint]. 2020. Available from: https://www.biorxiv.org/content/10.1101/2020.06.17.156455v1
60. Gill SE, dos Santos CC, O'Gorman DB, Carter DE, Patterson EK, Slessarev M, et al. Transcriptional profiling of leukocytes in critically ill COVID19 patients: implications for interferon response and coagulation. Intensive Care Medicine Experimental. 2020 Dec 11;8(1).
61. Gordon DE, Jang GM, Bouhaddou M, Xu J, Obernier K, White KM, et al. A SARS-CoV-2 protein interaction map reveals targets for drug repurposing. Nature. 2020 Jul 30;583(7816).
62. Li J, Guo M, Tian X, Wang X, Yang X, Wu P, et al. Virus-Host Interactome and Proteomic Survey Reveal Potential Virulence Factors Influencing SARS-CoV-2 Pathogenesis. Med. 2020 Jul;
63. Cruz JLG, Sola I, Becares M, Alberca B, Plana J, Enjuanes L, et al. Coronavirus Gene 7 Counteracts Host Defenses and Modulates Virus Virulence. PLoS Pathogens. 2011 Jun 9;7(6).
64. V'kovski P, Gerber M, Kelly J, Pfaender S, Ebert N, Braga Lagache S, et al. Determination of host proteins composing the microenvironment of coronavirus replicase complexes by proximity-labeling. eLife. 2019 Jan 11;8.
65. Chu H, Chan C-M, Zhang X, Wang Y, Yuan S, Zhou J, et al. Middle East respiratory syndrome coronavirus and bat coronavirus HKU9 both can utilize GRP78 for attachment onto host cells. Journal of Biological Chemistry. 2018 Jul 27;293(30).
66. Siu K-L, Chan C-P, Kok K-H, Woo PC-Y, Jin D-Y. Comparative analysis of the activation of unfolded protein response by spike proteins of severe acute respiratory syndrome coronavirus and human coronavirus HKU1. Cell & Bioscience. 2014;4(1).
67. Li S, Yuan L, Dai G, Chen RA, Liu DX, Fung TS. Regulation of the ER Stress Response by the Ion Channel Activity of the Infectious Bronchitis Coronavirus Envelope Protein Modulates Virion Release, Apoptosis, Viral Fitness, and Pathogenesis. Frontiers in Microbiology. 2020 Jan 24;10.
68. Xue M, Fu F, Ma Y, Zhang X, Li L, Feng L, et al. The PERK Arm of the Unfolded Protein Response Negatively Regulates Transmissible Gastroenteritis Virus Replication by Suppressing Protein Translation and Promoting Type I Interferon Production. Journal of Virology. 2018 May 16;92(15).
69. Wang X, Liao Y, Yap PL, Png KJ, Tam JP, Liu DX. Inhibition of Protein Kinase R Activation and Upregulation of GADD34 Expression Play a Synergistic Role in Facilitating Coronavirus Replication by Maintaining De Novo Protein Synthesis in Virus-Infected Cells. Journal of Virology. 2009 Dec 1;83(23).
70. Liao Y, Fung TS, Huang M, Fang SG, Zhong Y, Liu DX. Upregulation of CHOP/GADD153 during Coronavirus Infectious Bronchitis Virus Infection Modulates Apoptosis by Restricting Activation of the Extracellular Signal-Regulated Kinase Pathway. Journal of Virology. 2013 Jul 15;87(14).

71. DeDiego ML, Nieto-Torres JL, Jiménez-Guardeño JM, Regla-Nava JA, Álvarez E, Oliveros JC, et al. Severe Acute Respiratory Syndrome Coronavirus Envelope Protein Regulates Cell Stress Response and Apoptosis. PLoS Pathogens. 2011 Oct 20;7(10).
72. Krähling V, Stein DA, Spiegel M, Weber F, Mühlberger E. Severe Acute Respiratory Syndrome Coronavirus Triggers Apoptosis via Protein Kinase R but Is Resistant to Its Antiviral Activity. Journal of Virology. 2009 Mar 1;83(5).
73. Ye Z, Wong CK, Li P, Xie Y. A SARS-CoV protein, ORF-6, induces caspase-3 mediated, ER stress and JNK-dependent apoptosis. Biochimica et Biophysica Acta (BBA) - General Subjects. 2008 Dec;1780(12).
74. Shi C-S, Nabar NR, Huang N-N, Kehrl JH. SARS-Coronavirus Open Reading Frame-8b triggers intracellular stress pathways and activates NLRP3 inflammasomes. Cell Death Discovery. 2019 Dec 5;5(1).
75. Chen C-Y, Ping Y-H, Lee H-C, Chen K-H, Lee Y-M, Chan Y-J, et al. Open Reading Frame 8a of the Human Severe Acute Respiratory Syndrome Coronavirus Not Only Promotes Viral Replication but Also Induces Apoptosis. The Journal of Infectious Diseases. 2007 Aug 1;196(3).
76. Chan JF-W, Kok K-H, Zhu Z, Chu H, To KK-W, Yuan S, et al. Genomic characterization of the 2019 novel human-pathogenic coronavirus isolated from a patient with atypical pneumonia after visiting Wuhan. Emerging Microbes & Infections. 2020 Jan 1;9(1).
77. Young BE, Fong S-W, Chan Y-H, Mak T-M, Ang LW, Anderson DE, et al. Effects of a major deletion in the SARS-CoV-2 genome on the severity of infection and the inflammatory response: an observational cohort study. The Lancet. 2020 Aug;396(10251).
78. Su YCF, Anderson DE, Young BE, Linster M, Zhu F, Jayakumar J, et al. Discovery and Genomic Characterization of a 382-Nucleotide Deletion in ORF7b and ORF8 during the Early Evolution of SARS-CoV-2. mBio. 2020 Jul 21;11(4).
79. Gong Y-N, Tsao K-C, Hsiao M-J, Huang C-G, Huang P-N, Huang P-W, et al. SARS-CoV-2 genomic surveillance in Taiwan revealed novel ORF8-deletion mutant and clade possibly associated with infections in Middle East. Emerging Microbes & Infections. 2020 Jan 1;9(1).
80. Muth D, Corman VM, Roth H, Binger T, Dijkman R, Gottula LT, et al. Attenuation of replication by a 29 nucleotide deletion in SARS-coronavirus acquired during the early stages of human-to-human transmission. Scientific Reports. 2018 Dec 11;8(1).
81. Nakabo Y, Pabst MJ. Lysis of leukemic cells by human macrophages: inhibition by 4-(2-aminoethyl)-benzenesulfonyl fluoride (AEBSF), a serine protease inhibitor. Journal of Leukocyte Biology. 1996 Sep;60(3).
82. Barua S, Kim JY, Yenari MA, Lee JE. The role of NOX inhibitors in neurodegenerative diseases. IBRO Reports. 2019 Dec;7.
83. Thamsen M, Ghosh R, Auyeung VC, Brumwell A, Chapman HA, Backes BJ, et al. Small molecule inhibition of IRE1α kinase/RNase has anti-fibrotic effects in the lung. PLOS ONE. 2019 Jan 9;14(1).
84. Wang X, Xu M, Frank JA, Ke Z, Luo J. Thiamine deficiency induces endoplasmic reticulum stress and oxidative stress in human neurons derived from induced pluripotent stem cells. Toxicology and Applied Pharmacology. 2017 Apr;320.
85. Chien W, Ding L-W, Sun Q-Y, Torres-Fernandez LA, Tan SZ, Xiao J, et al. Selective inhibition of unfolded protein response induces apoptosis in pancreatic cancer cells. Oncotarget. 2014 Jul 15;5(13).
86. Bradley KL, Stokes CA, Marciniak SJ, Parker LC, Condliffe AM. Role of unfolded proteins in lung disease. Thorax. 2020 Oct 19.
87. Sureda A, Alizadeh J, Nabavi SF, Berindan-Neagoe I, Cismaru CA, Jeandet P, et al. Endoplasmic reticulum as a potential therapeutic target for covid-19 infection management? European Journal of Pharmacology. 2020 Sep;882.
88. Aoe T. Pathological Aspects of COVID-19 as a Conformational Disease and the Use of Pharmacological Chaperones as a Potential Therapeutic Strategy. Frontiers in Pharmacology. 2020 Jul 10;11.
89. Cimellaro A, Perticone M, Fiorentino TV, Sciacqua A, Hribal ML. Role of endoplasmic reticulum stress in endothelial dysfunction. Nutrition, Metabolism and Cardiovascular Diseases. 2016 Oct;26(10).

90. Lenna S, Han R, Trojanowska M. Endoplasmic reticulum stress and endothelial dysfunction. IUBMB Life. 2014 Aug;66(8).
91. Varga Z, Flammer AJ, Steiger P, Haberecker M, Andermatt R, Zinkernagel AS, et al. Endothelial cell infection and endotheliitis in COVID-19. The Lancet. 2020 May;395(10234).
92. Grasselli G, Tonetti T, Protti A, Langer T, Girardis M, Bellani G, et al. Pathophysiology of COVID-19-associated acute respiratory distress syndrome: a multicentre prospective observational study. The Lancet Respiratory Medicine. 2020 Dec;8(12).
93. Yang X, Yu Y, Xu J, Shu H, Xia J, Liu H, et al. Clinical course and outcomes of critically ill patients with SARS-CoV-2 pneumonia in Wuhan, China: a single-centered, retrospective, observational study. The Lancet Respiratory Medicine. 2020 May;8(5).
94. Gavriilaki E, Anyfanti P, Gavriilaki M, Lazaridis A, Douma S, Gkaliagkousi E. Endothelial Dysfunction in COVID-19: Lessons Learned from Coronaviruses. Current Hypertension Reports. 2020 Sep 27;22(9).
95. Grillo F, Barisione E, Ball L, Mastracci L, Fiocca R. Lung fibrosis: an undervalued finding in COVID-19 pathological series. The Lancet Infectious Diseases. 2020 Jul.
96. Huang W, Wu Q, Chen Z, Xiong Z, Wang K, Tian J, et al. The potential indicators for pulmonary fibrosis in survivors of severe COVID-19. Journal of Infection. 2020 Sep.
97. Burman A, Tanjore H, Blackwell TS. Endoplasmic reticulum stress in pulmonary fibrosis. Matrix Biology. 2018 Aug;68–69.
98. Sturman LS, Takemoto KK. Enhanced Growth of a Murine Coronavirus in Transformed Mouse Cells. Infection and Immunity. 1972;6(4).
99. Busnadiego I, Fernbach S, Pohl MO, Karakus U, Huber M, Trkola A, et al. Antiviral Activity of Type I, II, and III Interferons Counterbalances ACE2 Inducibility and Restricts SARS-CoV-2. mBio. 2020 Sep 10;11(5).
100. Pohl MO, Busnadiego I, Kufner V, Schmutz S, Zaheri M, Abela I, et al. Distinct Phenotypes of SARS-CoV-2 isolates reveal viral traits critical for replication in primary human respiratory cells. bioRxiv [Preprint]. 2020. Available from: https://www.biorxiv.org/content/10.1101/2020.10.22.350207v1
101. Chung BY, Hardcastle TJ, Jones JD, Irigoyen N, Firth AE, Baulcombe DC, et al. The use of duplex-specific nuclease in ribosome profiling and a user-friendly software package for Ribo-seq data analysis. RNA. 2015 Oct;21(10).
102. Quast C, Pruesse E, Yilmaz P, Gerken J, Schweer T, Yarza P, et al. The SILVA ribosomal RNA gene database project: improved data processing and web-based tools. Nucleic Acids Research. 2012 Nov 27;41(D1).
103. Dobin A, Davis CA, Schlesinger F, Drenkow J, Zaleski C, Jha S, et al. STAR: ultrafast universal RNA-seq aligner. Bioinformatics. 2013 Jan;29(1).
104. Anders S, Pyl PT, Huber W. HTSeq--a Python framework to work with high-throughput sequencing data. Bioinformatics. 2015 Jan 15;31(2).
105. Langmead B, Trapnell C, Pop M, Salzberg SL. Ultrafast and memory-efficient alignment of short DNA sequences to the human genome. Genome Biology. 2009;10(3).
106. Mi H, Muruganujan A, Huang X, Ebert D, Mills C, Guo X, et al. Protocol Update for large-scale genome and gene function analysis with the PANTHER classification system (v.14.0). Nature Protocols. 2019 Mar 25;14(3).

979 **Figure Captions:**
980

981 **Figure 1: Ribosome profiling reveals the unfolded protein response as a key pathway in**
982 **the host response to MHV-A59 infection. (A)** Schematic of the three branches of the UPR
983 (IRE1α, ATF6, and PERK). ERAD = ER-associated protein degradation. **(B)** Top five most
984 significantly enriched Reactome pathways[9] associated with the lists of transcriptionally up-
985 regulated genes (orange triangles pointing upwards) and transcriptionally down-regulated
986 genes (blue triangles pointing downwards), plotted according to the false discovery rate (FDR)-
987 corrected *p* value of the enrichment. Full results, including pathway IDs, are in Supplementary
988 Table 3. **(C)** Volcano plot showing the relative change in abundance of cellular transcripts and
989 the FDR-corrected *p* value for differential expression between the mock and infected samples
990 (n=2 biological replicates). Grey vertical lines indicate a transcript abundance fold change of
991 2. Genes which have fold changes greater than this threshold and a $p \leq 0.05$ value of less than
992 0.05 are considered significantly differentially expressed and coloured orange if up-regulated
993 and blue if down-regulated. Selected genes are annotated in red. **(D)** Volcano plot showing the
994 relative change in translation efficiency of cellular transcripts, and the FDR-corrected *p* value,
995 between the mock and infected samples (n=2 biological replicates). Colours and fold change
996 and *p* value thresholds as in C. **(E)** Analysis of RPFs mapping to *Atf4* (NCBI RefSeq mRNA
997 NM_009716). Cells were infected with MHV-A59 or mock-infected and harvested at 5 h p.i.
998 (libraries from replicate 2) or 8 h p.i. RPFs are plotted at the inferred position of the ribosomal
999 P site and coloured according to the phase of translation: pink for 0, blue for +1, yellow for +2.
1000 The main ORF (0 frame) is shown at the top in pink, with start and stop codons in all three
1001 frames marked by green and red bars (respectively) in the three panels below. The two yellow
1002 rectangles are in the +2 frame indicate the known *Atf4* uORFs (the first of which is only three
1003 codons in length). Dotted lines serve as markers for the start and end of the features in their
1004 matching colour. Note that read densities are plotted as reads per million host-mRNA-mapping

1005 reads, and that bar widths were increased to 12 nt to aid visibility, and therefore overlap, and
1006 were plotted sequentially starting from the 5′ end of the transcript. **(F)** Plot of $\log_2$(fold changes)
1007 of translation efficiency (TE) vs transcript abundance for all genes included in both analyses.
1008 Grey lines indicate fold changes of 2. Fold changes are plotted without filtering for significant
1009 *p* values. Selected genes are marked: genes up-regulated predominantly by one of either
1010 transcription or TE are marked in orange (upper middle and right middle sections), and *Chop*,
1011 which is up-regulated at the level of both transcription and TE, is marked in green (top right
1012 section).
1013
1014 **Figure 2: MHV infection and activation of the unfolded protein response.** 17 Cl-1 cells
1015 were incubated in the presence of tunicamycin (2 μg/ml) or infected with MHV-A59 (MOI 5)
1016 and harvested at 2.5, 5, 8 and 10 h p.i. **(A)** Cell lysates were separated by 12% SDS-PAGE and
1017 immunoblotted using anti-ATF4, anti-p-eIF2α, anti-eIF2α, anti-PERK and anti-N antibodies
1018 (green fluorescent secondary antibody). GAPDH was used as a loading control (red fluorescent
1019 secondary antibody). Molecular masses (kDa) are indicated on the left and the p-eIF2α band is
1020 indicated by a white asterisk. **(B)** RT-qPCR of *Chop* and *Gadd34* mRNA for three biological
1021 replicates of a timecourse of MHV infection or tunicamycin treatment. Data are normalised
1022 using *Rpl19* as a housekeeping gene and presented as fold change of expression relative to
1023 mock-infected cells (marked as a dashed line). **(C)** Mock-infected (left upper panel) and MHV-
1024 infected (right upper panel) 17 Cl-1 cells were harvested at 5 h p.i. Cytoplasmic lysates were
1025 resolved on 10–50% sucrose density gradients. Gradients were fractionated and fractions
1026 monitored by absorbance (A_{254} nm). Twelve numbered fractions were collected and proteins
1027 extracted, resolved by 12% SDS-PAGE and analysed by immunoblotting using the indicated
1028 antibodies (anti-S6 as 40S marker, anti-RPL10 as 60S marker). Mock-infected (left lower
1029 panel) and MHV-infected (right lower panel) 17 Cl-1 cells were harvested at 5 h p.i. in high-
1030 salt lysis buffer (400 mM KCl) and analysed as described above. Molecular masses (kDa) are

1031 indicated on the left. Lane "Inp" contains whole cell lysate. **(D)** RT-PCR analysis of *Xbp1-u*
1032 and *Xbp1-s* mRNAs. Total RNA (0.5µg) was subjected to RT-PCR analysis using primers
1033 flanking the *Xbp1* splice site. PCR products were resolved in a 3% TBE-agarose gel and
1034 visualised by ethidium bromide staining. *Rpl19* RT-PCR product was used as a loading control.
1035 Molecular size markers (nt) are indicated on the left. **(E)** RT-qPCR of *Bip*, *calreticulin* and
1036 *Grp94* mRNA for three biological replicates of a timecourse of MHV infection or tunicamycin
1037 treatment. Data are normalised as in B. (**F**) Cell lysates were analysed by 12% SDS-PAGE and
1038 immunoblotted using anti-BiP and anti-N antibodies. GAPDH was used as a loading control.
1039
1040 **Figure 3: Effect of UPR inhibitors on MHV replication.** (**A**) MHV-infected cells (MOI 5)
1041 were treated with UPR inhibitors (5 µM PERKi, 2 µM ISRIB, 60 µM IREi, or 100 µM
1042 AEBSF). The inhibitors were added to the cells immediately after the virus adsorption period
1043 and maintained in the medium until cells were harvested 8 h later. Plaque assays were
1044 performed with serial dilutions of the supernatant containing released virions from 17 Cl-1
1045 cells infected with MHV-A59 in the presence or absence of the UPR inhibitors. Values show
1046 the mean averages of the titration of three biological replicates. Error bars represent standard
1047 errors. **(B-D)** MHV-infected cells (MOI 1 and MOI 5) were treated with dual combinations of
1048 the UPR inhibitors. The inhibitors were added to the cells immediately after the virus
1049 adsorption period and maintained in the medium until cells were harvested 8 h later. (**B**)
1050 Released virions were quantified as described in A. (**C**) Cell lysates were separated by 12%
1051 SDS-PAGE and immunoblotted using anti-N and anti-GAPDH antibodies as described in Fig
1052 2A. (**D**) Representative images of mock- and MHV-infected cells at 8 h p.i. under no-drug or
1053 IREi 60 µM/AEBSF 100µM treatment conditions. All *t*-tests were two-tailed and did not
1054 assume equal variance for the two populations being compared (*$p < 0.05$, ** $p < 0.01$, ***

1055 $p < 0.001$, **** $p < 0.0001$). All p-values are from comparisons with the respective no-
1056 treatment control at the same MOI.
1057
1058 **Figure 4: Mechanistic analysis of UPR activation by SARS-CoV-2 proteins.** HEK-293T
1059 cells were transfected with plasmids encoding SARS-CoV 2 S (S-HA) or ORF8 (ORF8-
1060 FLAG), mock-transfected, or treated with tunicamycin (Tn). At 8 h p.t., cells were treated with
1061 60 μM IREi and 100 μM AEBSF and then harvested at 24 and 36 h p.t. (**A**) Cells were harvested
1062 at 24 and 36 h p.t. and cell lysates were separated by 12% SDS-PAGE and immunoblotted
1063 using anti-FLAG, anti-HA, anti-HERP, anti-BiP, anti-PERK, anti-ATF4, anti-p-eIF2α, anti-
1064 eIF2α and anti-ATF6 as described in Fig 2A. The specific p-eIF2α and ATF6-Nt bands are
1065 indicated with a white asterisk. (**B**) RT-PCR analysis of *XBP1-u* and *XBP1-s* mRNAs as
1066 described in Fig 2D. "h p.t." = hours post-transfection.
1067
1068 **Figure 5: Induction of the UPR in SARS-CoV-2 infected cells and the effect of UPRi.** Vero
1069 CCL81 cells were incubated in the presence of tunicamycin (2 μg/ml) or infected with SARS-
1070 CoV-2 (MOI 1) and treated with 60 μM IREi and 100 μM AEBSF. The inhibitors were added
1071 to the cells immediately after the virus adsorption period and maintained in the medium until
1072 cells were harvested 24 and 48 h later. (**A**) Cell lysates (upper) were immunoblotted using anti-
1073 S, anti-BiP, anti-HERP, anti-PERK, anti-ATF4, anti-p-eIF2α, anti-eIF2α, anti-ATF6 and anti-
1074 GAPDH antibodies as described in Fig 2A. RT-PCR analysis of *Xbp1-u* and *Xbp1-s* mRNAs
1075 (lower) as described in Fig 2D. The specific p-eIF2α and ATF6-Nt bands are indicated with a
1076 white asterisk. (**B**) $TCID_{50}$ assays were performed with serial dilutions of the supernatant
1077 containing released virions from Caco2 cells infected with SARS-CoV-2 (MOI 0.01) for 48 h
1078 in the presence or absence of the indicated UPRi combinations. (**C**) Plaque assays were
1079 performed with serial dilutions of the supernatant containing released virions from Vero
1080 CCL81 or Calu3 cells infected with SARS-CoV-2 (MOI 1 and MOI 5) for 24 h in the presence

1081 or absence of 60 μM IREi and 100 μM AEBSF. Values show the mean averages of the titration
1082 of three biological replicates. Error bars represent standard errors. All *t*-tests were two-tailed
1083 and did not assume equal variance for the two populations being compared (*$p < 0.05$, **
1084 $p < 0.01$). Replicates with titres below the limit of detection (LoD) were excluded from *t*-tests,
1085 precluding some conditions from statistical assessment.

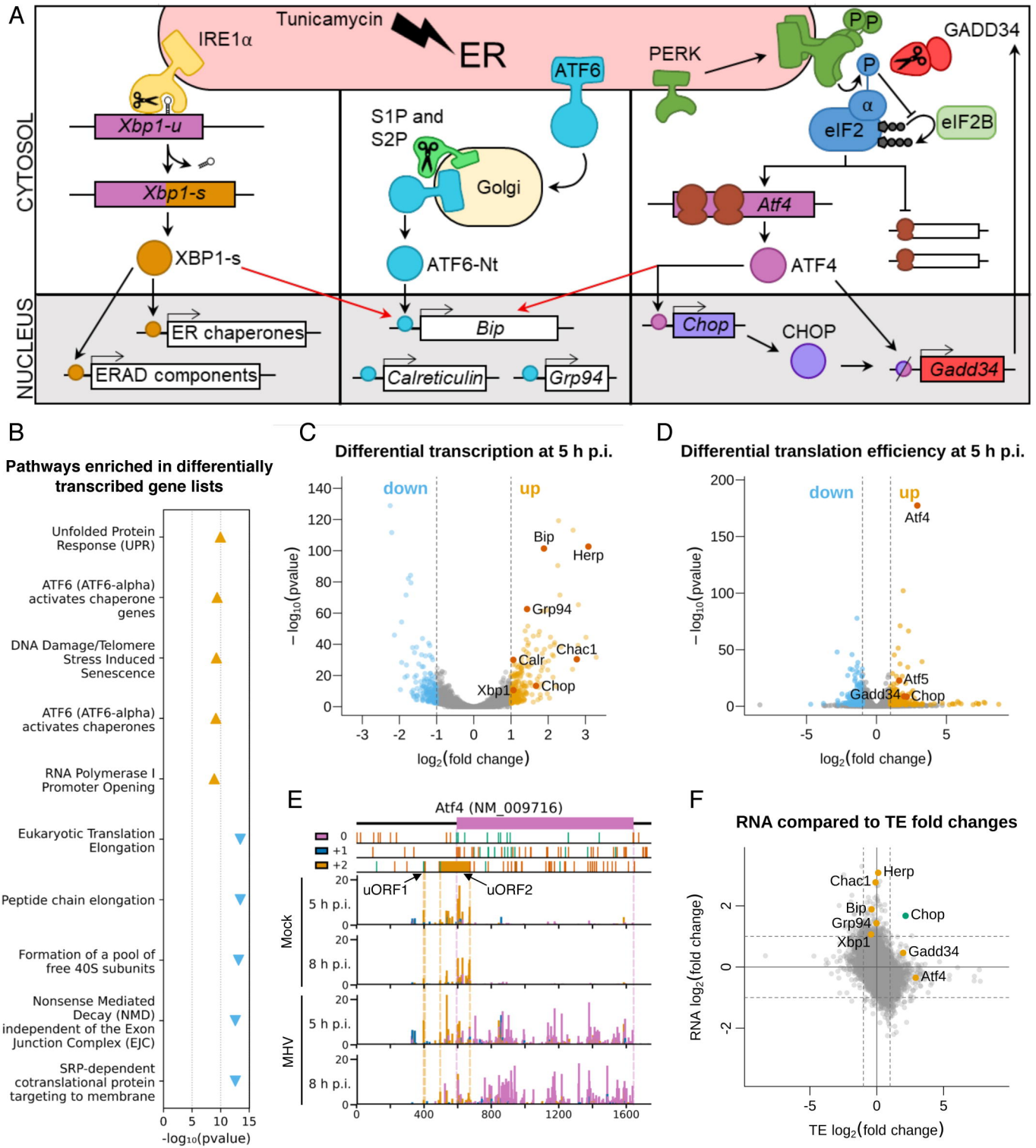
A
Tunicamycin
ER
IRE1α
ATF6
PERK
GADD34
CYTOSOL
NUCLEUS
Xbp1-u
Xbp1-s
XBP1-s
S1P and
S2P
Golgi
ATF6-Nt
eIF2
eIF2B
Atf4
ATF4
ER chaperones
ERAD components
Bip
Calreticulin
Grp94
Chop
CHOP
Gadd34
B
Pathways enriched in differentially transcribed gene lists
Unfolded Protein Response (UPR)
ATF6 (ATF6-alpha) activates chaperone genes
DNA Damage/Telomere Stress Induced Senescence
ATF6 (ATF6-alpha) activates chaperones
RNA Polymerase I Promoter Opening
Eukaryotic Translation Elongation
Peptide chain elongation
Formation of a pool of free 40S subunits
Nonsense Mediated Decay (NMD) independent of the Exon Junction Complex (EJC)
SRP-dependent cotranslational protein targeting to membrane
-log10(pvalue)
C
Differential transcription at 5 h p.i.
down
up
Bip
Herp
Grp94
Chac1
Calr
Xbp1
Chop
−log10(pvalue)
log2(fold change)
D
Differential translation efficiency at 5 h p.i.
down
up
Atf4
Atf5
Gadd34
Chop
−log10(pvalue)
log2(fold change)
E
Atf4 (NM_009716)
uORF1
uORF2
Mock
MHV
5 h p.i.
8 h p.i.
F
RNA compared to TE fold changes
Chac1
Herp
Bip
Chop
Grp94
Xbp1
Gadd34
Atf4
RNA log2(fold change)
TE log2(fold change)

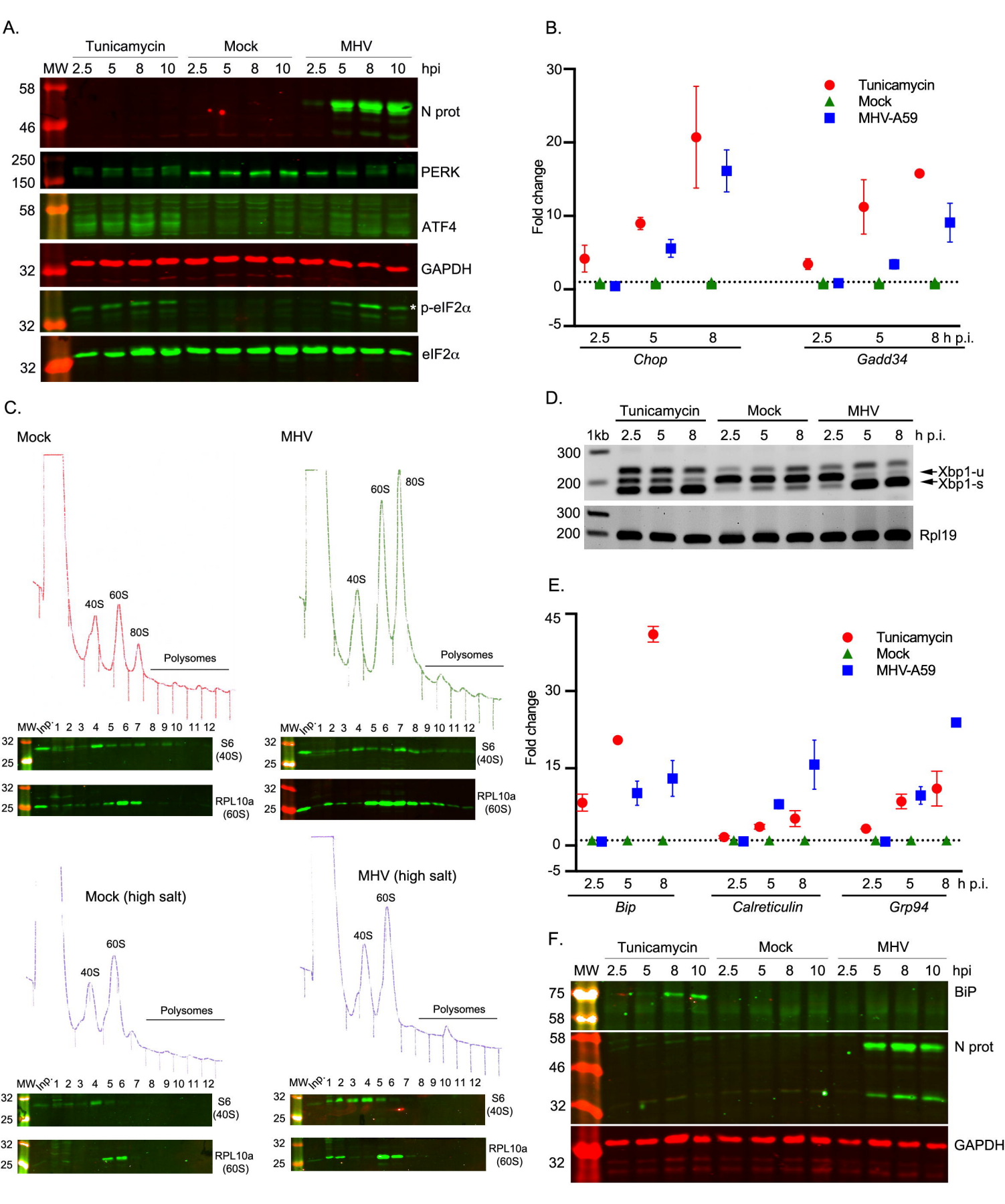
A.
Tunicamycin
Mock
MHV
MW 2.5 5 8 10 2.5 5 8 10 2.5 5 8 10 hpi
58
46
N prot
250
150
PERK
58
ATF4
32
GAPDH
32
* p-eIF2α
32
eIF2α
B.
Tunicamycin
Mock
MHV-A59
Fold change
30
20
10
0
-5
2.5 5 8 2.5 5 8 h p.i.
Chop
Gadd34
C.
Mock
MHV
40S
60S
80S
Polysomes
MW Inp 1 2 3 4 5 6 7 8 9 10 11 12
32
25
S6 (40S)
RPL10a (60S)
Mock (high salt)
MHV (high salt)
D.
Tunicamycin
Mock
MHV
1kb 2.5 5 8 2.5 5 8 2.5 5 8 h p.i.
300
200
Xbp1-u
Xbp1-s
Rpl19
E.
Tunicamycin
Mock
MHV-A59
Fold change
45
30
15
0
-5
2.5 5 8 2.5 5 8 2.5 5 8 h p.i.
Bip
Calreticulin
Grp94
F.
Tunicamycin
Mock
MHV
MW 2.5 5 8 10 2.5 5 8 10 2.5 5 8 10 hpi
75
58
BiP
58
46
32
N prot
32
GAPDH

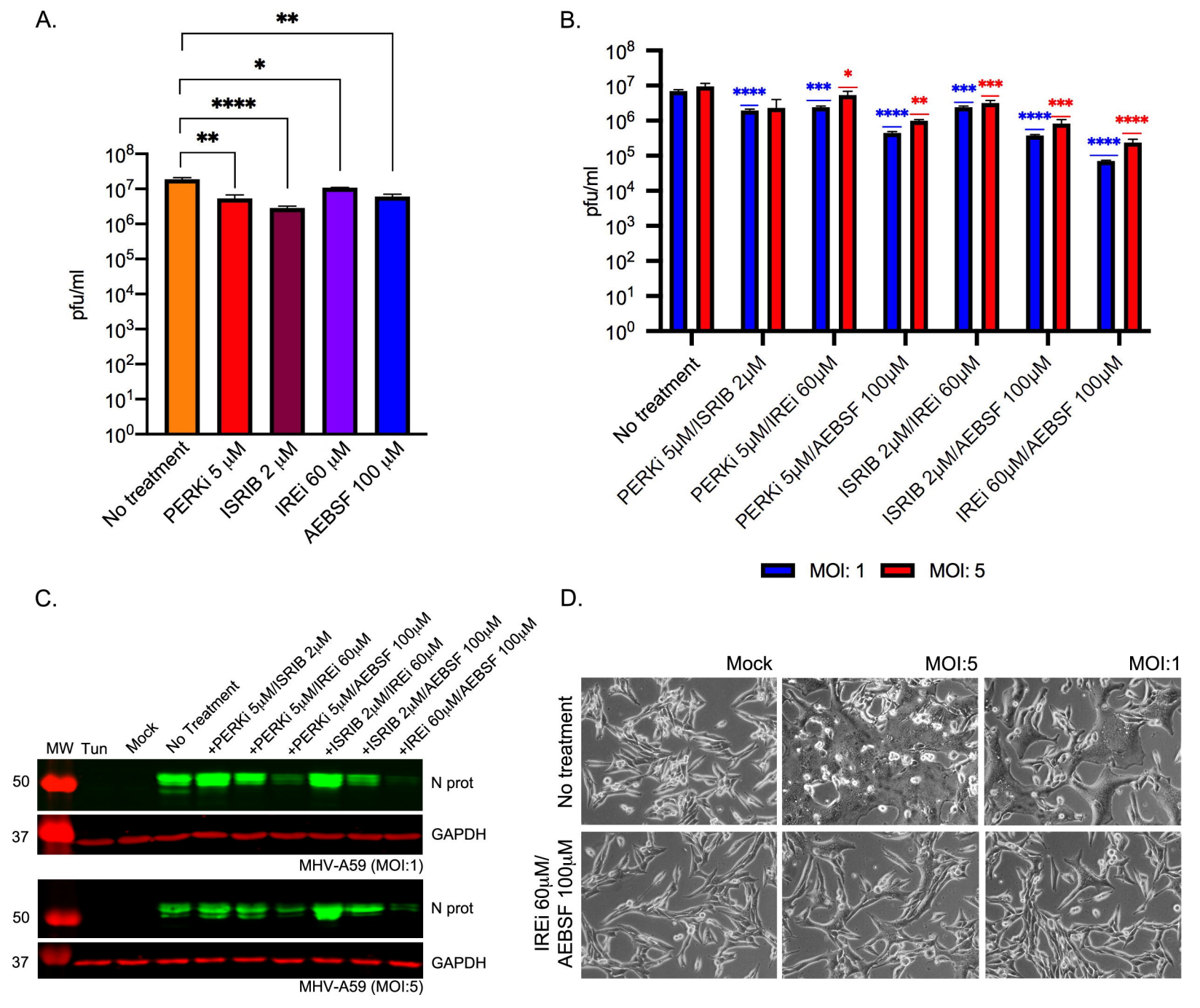
A.
pfu/ml
No treatment
PERKi 5 μM
ISRIB 2 μM
IREi 60 μM
AEBSF 100 μM
B.
pfu/ml
No treatment
PERKi 5μM/ISRIB 2μM
PERKi 5μM/IREi 60μM
PERKi 5μM/AEBSF 100μM
ISRIB 2μM/IREi 60μM
ISRIB 2μM/AEBSF 100μM
IREi 60μM/AEBSF 100μM
MOI: 1
MOI: 5
C.
MW
Tun
Mock
No Treatment
+PERKi 5μM/ISRIB 2μM
+PERKi 5μM/IREi 60μM
+PERKi 5μM/AEBSF 100μM
+ISRIB 2μM/IREi 60μM
+ISRIB 2μM/AEBSF 100μM
+IREi 60μM/AEBSF 100μM
50
37
N prot
GAPDH
MHV-A59 (MOI:1)
MHV-A59 (MOI:5)
D.
Mock
MOI:5
MOI:1
No treatment
IREi 60μM/
AEBSF 100μM

A.

24 h p.t. | 36 h p.t.

MW Tn | Mock | S prot | ORF8 | Mock | S prot | ORF8 | IREi/AEBSF

- + - + - + - +

S -HA

150
100
75
50

20
15

ORF8-FLAG

ER stress

75
50

HERP

75

BiP

PERK-eIF2α-ATF4 branch

100

PERK

50

ATF4

37

p-eIF2α *

37

eIF2α

ATF6-branch

100
75
50

ATF6

ATF6-Nt *

B.

24 h p.t. | 36 h p.t.

1kb Tn | Mock | S prot | ORF8 | Mock | S prot | ORF8 | IREi/AEBSF

- + - + - + - +

200
100

Xbp1-u
Xbp1-s

200
100

Rpl19

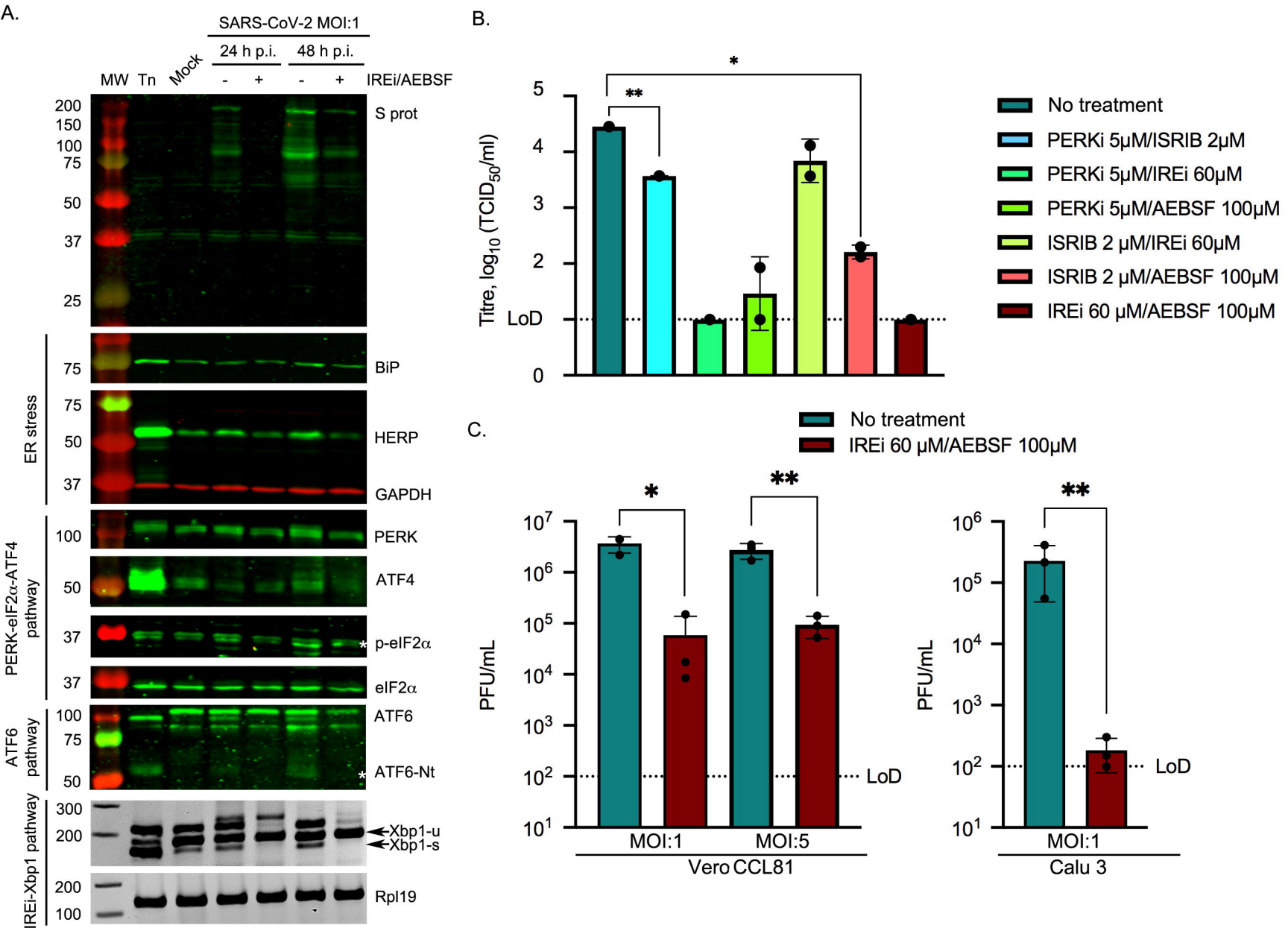
A.
SARS-CoV-2 MOI:1
24 h p.i.
48 h p.i.
MW
Tn
Mock
-
+
-
+
IREi/AEBSF
200
150
100
75
50
37
25
S prot
ER stress
75
BiP
75
50
37
HERP
GAPDH
PERK-eIF2α-ATF4 pathway
100
PERK
50
ATF4
37
p-eIF2α
37
eIF2α
ATF6 pathway
100
75
50
ATF6
ATF6-Nt
IREi-Xbp1 pathway
300
200
Xbp1-u
Xbp1-s
200
100
Rpl19
B.
Titre, log10 (TCID50/ml)
5
4
3
2
LoD
0
*
**
No treatment
PERKi 5μM/ISRIB 2μM
PERKi 5μM/IREi 60μM
PERKi 5μM/AEBSF 100μM
ISRIB 2 μM/IREi 60μM
ISRIB 2 μM/AEBSF 100μM
IREi 60 μM/AEBSF 100μM
C.
No treatment
IREi 60 μM/AEBSF 100μM
PFU/mL
10^7
10^6
10^5
10^4
10^3
10^2
10^1
LoD
MOI:1
MOI:5
Vero CCL81
Calu 3